Precise velocity differences turn 100 wide binaries into a conditional test of gravity.

Draft version December 23, 2025
Typeset using LaTeX **twocolumn** style in AASTeX7.0.1

arXiv:2512.19652v1 [astro-ph.SR] 22 Dec 2025

High-Precision Differential Radial Velocities of C3PO Wide Binaries: A Test of Modified Newtonian Dynamics (MOND)

Serat Mahmud Saad [1] and Yuan-Sen Ting [1,2]

[1] Department of Astronomy, The Ohio State University, 140 W. 18th Ave., Columbus, OH 43210, USA
[2] Department of Astronomy and Center for Cosmology and AstroParticle Physics, The Ohio State University, 140 W. 18th Ave, Columbus, OH, 43210, USA

ABSTRACT

Wide-binary stars, separated by thousands of AU, reside in low-acceleration regimes where Modified Newtonian Dynamics (MOND) predicts deviation from Newtonian gravity. However, *Gaia* radial velocities (RVs) lack the precision to resolve the small velocity differences expected in these systems, limiting previous MOND analyses to two-dimensional kinematics. In this paper, we introduce a technique to measure differential RVs of wide binary stars using high resolution, high signal-to-noise spectra. We apply this method to measure differential RVs of 100 wide-binaries from the C3PO survey and achieved precisions of ∼8–15 m s^{-1} per binary pair, a ∼10–100× improvement (median ∼ 24×) over *Gaia* DR3. Combining these measurements with *Gaia* astrometry, we construct a hierarchical Bayesian model to infer the orbital elements of all wide-binary pairs and the global MOND acceleration scale (a_0). We test two commonly used interpolating functions in MOND formulation: the simple form ($b = 1$, $\mu = x/(1+x)$) and the standard form ($b = 2$, $\mu = x/\sqrt{1+x^2}$). Our results indicate tension with MOND at the presently accepted a_0 value: for $b = 1$, the canonical value is excluded at 3.1σ, while for $b = 2$, the exclusion is at 1.9σ.

The reported tension with canonical MOND is stronger for the simple interpolation than for the standard form.

Keywords: gravitation — methods: statistical — techniques: radial velocities — binaries: visual — stars: kinematics and dynamics

1. INTRODUCTION

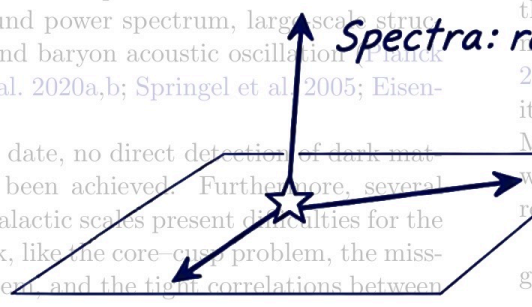
The physics of gravity in low acceleration regime remains one of the unsolved problems in science. Since the last century, evidence has indicated that the dynamics of galaxies and large-scale structures cannot be explained by visible matter alone under Newtonian gravity (Zwicky 1937; Rubin & Ford 1970; Rubin et al. 1980; Begeman 1989; Sofue & Rubin 2001). To address this discrepancy, the standard cosmological paradigm (λCDM) includes Cold Dark Matter (CDM) as the component which constitutes most of the mass of galaxies and galaxy clusters. λCDM framework has a number of successes like accurate predictions of the cosmic microwave background power spectrum, large-scale structure formation, and baryon acoustic oscillation (Planck Collaboration et al. 2020a,b; Springel et al. 2005; Eisenstein et al. 2005).

Nonetheless, to date, no direct detection of dark matter particles has been achieved. Furthermore, several observations on galactic scales present difficulties for the λCDM framework, like the core–cusp problem, the missing satellite problem, and the tight correlations between baryonic and dynamical properties of galaxies (Weinberg et al. 2015; Bullock & Boylan-Kolchin 2017). Although many of these issues may potentially be explained by baryon physics (Pontzen & Governato 2012; Di Cintio et al. 2014; Wetzel et al. 2016; Hopkins 2018).

As an alternative to dark matter, Milgrom (1983a) proposed Modified Newtonian Dynamics (MOND). MOND provides a modification of Newtonian gravity in the regime where accelerations fall below a scale of $a_0 \approx 1.2 \times 10^{-10}$ ms^{-2} (Milgrom 1983a,b). MOND can reproduce the flat rotation curves of spiral galaxies, the baryonic Tully-Fisher relation, and the internal dynamics of low-surface-brightness galaxies using only the universal parameter a_0 and without invoking dark matter (Sanders & McGaugh 2002; Famaey & McGaugh 2012; McGaugh 2016; Lelli et al. 2016). To predict gravitational lensing and cosmological observables properly, MOND was later embedded in Lagrangian-based frameworks like AQUAL (Bekenstein & Milgrom 1984) and relativistic extensions like TeVeS (Bekenstein 2004a).

However, MOND also faces challenges at the scale of galaxy clusters and cosmology where additional mass be-

An 8–15 m/s pairwise precision opens the line-of-sight dimension of the orbit.



Together: relative velocity in 3D

The missing ingredient is a precise line-of-sight velocity difference.

yond baryons seems required even in MOND framework (Sanders 2003; Angus 2008). This has motivated tests of MOND in environments different from galactic rotation curves, like wide binary stars in the solar neighborhood (Hernandez et al. 2012; Banik & Zhao 2018; Pittordis & Sutherland 2018). These wide binary stars, separated by thousands of AU, have gravitational acceleration in the scale of a_0, which is a suitable low acceleration regime to test MOND. On top of that, wide binaries should contain negligible dark matter even in the CDM paradigm, as the local dark matter density contributes only one part in $\sim 10^5$ of the binary's total mass within the orbit (Hernandez 2023). This makes testing MOND with wide-binaries independent of dark matter assumptions.

Since its inception, *Gaia* has provided precise astrometric data of billions of stars (Gaia Collaboration et al. 2016, 2021, 2023). This has enabled the identification of large samples of co-moving wide-binary pairs through their sky-projected relative velocities (Oh et al. 2017; El-Badry & Rix 2018; Hartman & Lépine 2020; Tian et al. 2020; El-Badry et al. 2021). Several initiatives have been taken to use *Gaia* wide binaries data to test MOND, which ended up in conflicting results. Hernandez et al. (2022); Hernandez (2023); Hernandez et al. (2024b) and Chae (2023, 2024a,b) have found evidence for gravitational anomaly consistent with MOND predictions at separations beyond ∼2–3 kAU. On the other hand, Pittordis & Sutherland (2023) and Banik et al. (2024) found the wide binary systems follow Newtonian gravity more than MOND. In a review by Hernandez et al. (2024a), it was argued that different modeling techniques, like treating hidden triple systems or inclusion of Newtonian calibration, were the reason of getting conflicting results in different studies.

A limitation of existing tests is their reliance on sky-projected relative velocities derived from *Gaia* proper motions. Though *Gaia* also provides radial velocities (RVs), their uncertainties are typically $\sim 1000\ \mathrm{m\,s^{-1}}$ (Katz et al. 2023), exceeding the expected velocity differences of ~ 50–$200\ \mathrm{m\,s^{-1}}$ in these wide binaries. Such RV uncertainties lack the statistical power to distinguish between MOND and Newtonian model. Beyond this, the absence of precise RVs prevents constraints on the full three-dimensional kinematics of these systems.

As discussed by El-Badry (2019), comparing the distribution of observed velocities to forward-simulated predictions under different gravity models has limited ability to validate individual systems, identify outliers, or propagate uncertainties from orbital degeneracies. In such case, a hierarchical Bayesian inference is necessary to fit orbital elements for each system along with global parameters like a_0. But this requires precise RV measurement to constrain individual orbits.

The theoretical precision limit for RV measurements can be estimated from the Cramér-Rao bound (Rao et al. 1945). For a spectrum with flux $F(\lambda)$, the minimum RV uncertainty scales as $\sigma_v \propto (\mathrm{SNR})^{-1}(\sum_i |\partial F_i/\partial\lambda|^2)^{-1/2}$, where the sum runs over spectral pixels (Bouchy et al. 2001). For *Gaia* RVS spectra ($R \approx 11500$, SNR $\sim$ 20–50 per transit, wavelength coverage of 845–872 nm), this yields uncertainties of ∼500–2000 $\mathrm{m\,s^{-1}}$ for solar-type stars. In contrast, high-resolution echelle spectra ($R \approx 50000$, SNR ∼150–300, spanning 3500–9000 Å) contain more spectral information. Our observations improve on all three factors that determine RV precision: spectral resolution R, SNR, and wavelength coverage (the number of spectral lines), achieving final differential RV precisions of ∼8–15 $\mathrm{m\,s^{-1}}$ per binary pair (see Section 2).

The Complete Census of Co-moving Pairs of Stars (C3PO) survey was designed to collect the largest sample of high resolution, high signal-to-noise ration (SNR) spectra of co-moving wide-binaries to date (Yong et al. 2023). Previous C3PO projects searched for planet engulfment in co-natal wide-binaries, where one star served as a chemical control for the other (Liu et al. 2024; Sun et al. 2025b; Yu et al. 2025; Sun et al. 2025a). Particularly, C3PO II (Liu et al. 2024) applied Bayesian model comparison to test whether observed abundance patterns were more consistent with a flat baseline, atomic diffusion, or planetary ingestion. This analysis identified eight planet-engulfment candidates among all the C3PO sources. Though C3PO was originally motivated by chemical abundance science, the same high-resolution, high SNR spectra also enable precise RV measurements. These precise RVs allows for a precision test of MOND.

In this paper, we test MOND using differential RV measurements of C3PO wide binaries. In section 2, we describe the C3PO dataset and the differential RV measurement technique. In section 3, we present the MOND formulation, geometry, and all the observable quantities that we adopt for this work. In section 4, we present the model framework, inference steps, and the posterior results of our analysis. Finally, in section 5, we discuss the implications of our findings along with their relevance to the ongoing efforts to test MOND, and possible future works.

2. DATA & MEASUREMENTS

2.1. *Data*

The C3PO survey collected high resolution, high SNR spectra of 125 co-moving star pairs (250 stars in total). To construct the C3PO sample spatial separa-

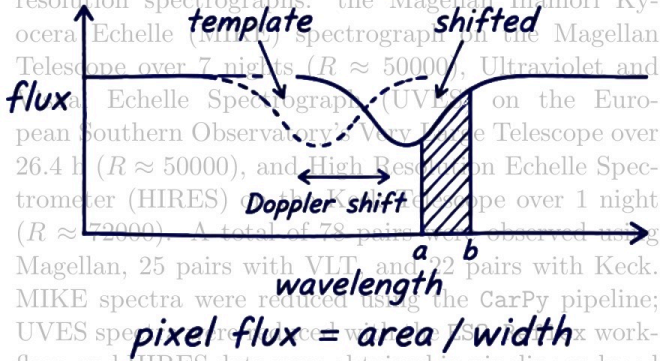
Proper motions capture only the sky-plane components; noisy radial velocities leave orbital ambiguities.

High resolution, high signal-to-noise and broad wavelength coverage all improve the velocity information.

One star becomes the spectral template for its companion, with the model integrated over each pixel.

tions and 3D velocity separations were first measured for co-moving pairs in *Gaia* DR3 (Gaia Collaboration et al. 2023) data using similar approach to Nelson et al. (2021). Constraints were then applied to spatial separations ($\Delta s < 10^{6.8}$ AU) and 3D velocity separations ($\Delta v < 2$ km s^{-1}) to limit contamination from non-co-natal pairs. Then additional photometric cuts were applied in the following way: (i) Color ($0.65 \leq$ BP $-$ RP ≤ 1.15 mag and $|\Delta$BP $-$ RP$| < 0.15$ mag), to ensure the homogeneity in the stellar type; (ii) Brightness (G mag < 10 mag), to ensure high SNR with low telescope time for precise spectroscopic measurement; and (iii) Absolute Magnitude ($\Delta M_G < 1$ mag), to ensure similarity in intrinsic luminosity between the binary pairs. Because of the color selection, the resulting C3PO sample is mostly consists of F, G, and K dwarfs with possible mass range from 0.8–1.2 $M_\odot$. The metallicity distribution spans approximately -0.5 to $+0.3$ dex, which represents the nearby thin-disk population. Because all C3PO targets are bright ($G < 10$ mag), the per-pixel SNR ranges from 150 to 300. We also used astrometry for all the C3PO sources from *Gaia*, including parallaxes, proper motion, and RVs with their uncertainties. Though we did not use the *Gaia* RVs directly, we used them to verify consistency with our measurements.

Shift, then average each pixel



pixel flux = area / width

All the spectroscopic data used in this work were high-resolution spectrographs: the Magellan Inamori Kyocera Echelle (MIKE) spectrograph on the Magellan Telescope over 7 nights ($R \approx 50000$), Ultraviolet and Visual Echelle Spectrograph (UVES) on the European Southern Observatory's Very Large Telescope over 26.4 h ($R \approx 50000$), and High Resolution Echelle Spectrometer (HIRES) on the Keck I Telescope over 1 night ($R \approx 72000$). A total of 78 pairs were observed using Magellan, 25 pairs with VLT, and 22 pairs with Keck. MIKE spectra were reduced using the `CarPy` pipeline; UVES spectra were reduced with the ESO Reflex workflow; and HIRES data were obtained in pipeline-reduced form from the Keck Observatory Archive (Bernstein et al. 2003; D'Odorico et al. 2000; Vogt et al. 1994). For all instruments, we used wavelength calibrated, blaze-corrected, order-by-order extracted 1-D spectra produced by the respective pipelines. Our final analysis includes 100 pairs (200 stars) from the C3PO survey from the original 125 pairs. We excluded the 22 Keck/HIRES pairs entirely because pipeline-reduced 1-D echelle spectra were not available for them. An additional 3 pairs from Magellan/MIKE and VLT/UVES were excluded because their extracted 1-D spectra were noisy for reliable differential RV measurements and would require re-reduction from raw frames.

Selection leaves 100 usable pairs from 125; this is a bright, similar-spectrum sample.

2.2. *Differential Radial Velocity*

Pairwise comparison cancels shared effects, while residual stellar and instrumental offests still need checking.

Measuring absolute RVs at the ~ 10 m s^{-1} level is challenging due to systematics including wavelength calibration errors, spectrograph drift, and astrophysical effects such as convective blueshift and gravitational redshift. For wide binaries observed with the same instrument under similar conditions, many of these systematics cancel when measuring differential RVs between the two components. This has a similar philosophy to the differential abundance technique in stellar spectroscopy, where comparing chemically similar stars observed in identical conditions yields more precise relative abundances (Meléndez et al. 2009; Bedell et al. 2018).

To measure differential RVs between wide-binary components, we developed a forward-modeling approach that accounts for the pixel-integrated nature of the echelle spectroscopy. Rather than cross-correlating flux samples directly, we designated one star in each pair as the template and the other as the comparison. For each echelle order of the template spectrum, we fitted a cubic spline. From this spline we computed a cumulative flux function $C(\lambda)$ to rapidly evaluate pixel-integrated model fluxes. For a trial velocity shift v, the comparison wavelength are related to the template wavelengths through a Doppler factor, $s = 1 + v/c$. The model flux for an observed pixel with wavelength boundaries $[a_i, b_i]$ is then,

$$F_i^{\rm mod}(v) = s\,\frac{C(b_i/s) - C(a_i/s)}{b_i - a_i} \tag{1}$$

This provides the photon-weighted flux, integrated over each detector pixel. We then evaluated a chi-squared statistic:

$$\chi^2(v) = \sum_i W_i\,\left[F_i^{\rm obs} - F_i^{\rm mod}(v)\right]^2 \tag{2}$$

where W_i are inverse-variance weights. This chi-squared was calculated over a velocity grid from -5 to $+5$ km s^{-1} in steps of 4 m s^{-1}. This grid spacing of 4 m s^{-1} is adequate for our analysis as it provides $\sim$5–10 times better resolution than our per-order Cramér-Rao bound, ensuring the grid discretization does not limit our precision. We determined the best-fit RV shift for each order as the velocity minimizing χ^2. This procedure yielded one differential RV measurement per echelle order. We estimate final uncertainties through bootstrap resampling rather than per-order error propagation, as described below.

For bootstrap resampling, we drew N orders with replacement (N = number of valid orders), compute median of that bootstrap sample, and repeat this for 10,000 iterations. The final differential RV was taken

Many spectral orders combine into one robust velocity difference for each pair.

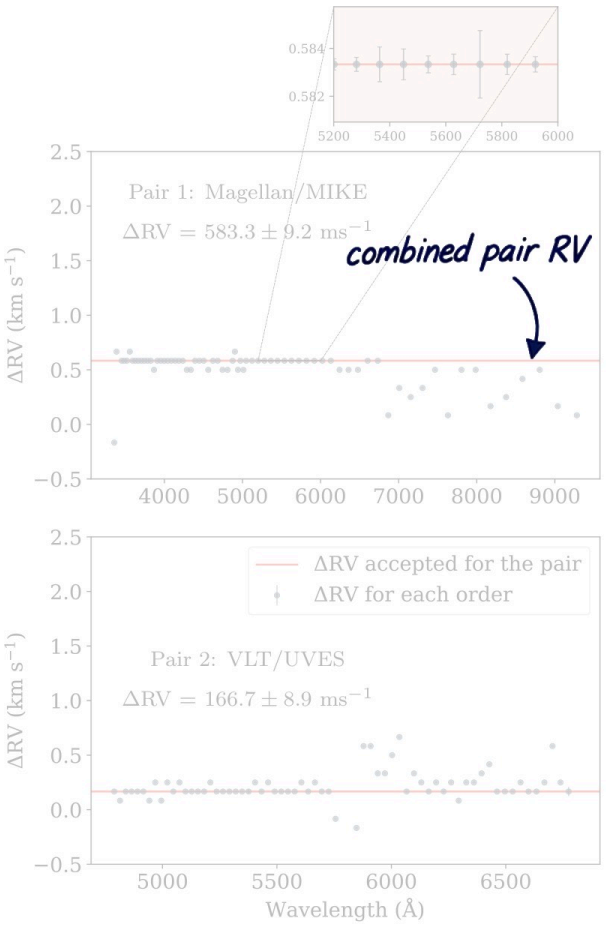


Figure 1. Per-order differential RV measurements as a function of wavelength for two representative wide-binary pairs. *Top panel:* Magellan/MIKE observations of the pair Gaia DR3 6473063860275183616 and Gaia DR3 6472230636619614464. The small plot above shows a zoomed in region of this plot. *Bottom panel:* VLT/UVES observations of the pair Gaia DR3 2919963104221492480 and Gaia DR3 2919963104216198528. Each point represents the ΔRV measured from a single echelle order, with error bars showing the 1σ uncertainty estimated from the χ^2 curve. The horizontal red line indicates the combined ΔRV obtained from bootstrap resampling of the median, which down-weights outlying orders without requiring sigma clipping.

as the median of the bootstrap distribution, while the standard deviation of the distribution gave us an estimate of the uncertainty in differential RV. The differential RV between the components of each binary is then $\Delta\mathrm{RV} = \mathrm{RV_B} - \mathrm{RV_A}$. The high SNR and high-resolution of the C3PO spectra returned per-order RV precisions of 20–40 $\mathrm{m\,s^{-1}}$ for most pairs. This improvement over Gaia follows from the Cramér-Rao scaling: our spectra have higher resolution (R ≈ 50,000 vs 11,500), higher SNR (∼150–300 vs ≈20–50), and broader wavelength coverage (3500–9000 Åvs 845–872 nm, providing ∼ 10× more spectral lines). Combining across ∼30—50 valid echelle orders yields final differential RV precisions of ∼8—15 $\mathrm{m\ s^{-1}}$ per binary pair.

The median is bootstrapped across orders; the spread of that bootstrap estimates the final uncertainty.

To demonstrate the improvement in statistical precision we compared our differential RVs to those derived from *Gaia* for the 84 pairs with available *Gaia* RV measurements. Measured RVs along with their instrument name, *Gaia* ID and *Gaia* proper motion info are given for a few of the sources in Table 1. Figure 1 shows the per-order differential RV measurements as a function of wavelength for two representative binary pairs observed with Magellan/MIKE and VLT/UVES. On Figure 2, the left plot shows the distribution of our uncertainties plotted alongside the *Gaia* uncertainties for all the 84 sources and the right plot shows the ratio of *Gaia* to our uncertainties, demonstrating a median improvement factor of ∼ 24. As Fisher information scales as σ^{-2}, this precision improvement translates directly to increased statistical power for constraining gravity models.

3. MOND ORBITS AND GEOMETRY

3.1. *MOND formulation*

According to Milgrom's original MOND formulation (Milgrom 1983a), gravitational acceleration is modified when it falls below a scale of $a_0 \approx 1.2 \times 10^{-10}$ $\mathrm{m\ s^{-2}}$. This modification is implemented through an interpolating function that transitions smoothly between the Newtonian and MOND regimes. We consider a generalized interpolating function of the form,

$$\mu(x) = \frac{x}{(1 + x^b)^{1/b}} \tag{3}$$

where $x = a/a_0$ is the acceleration in units of a_0, and b is a sharpness parameter controlling the transition. Two commonly used forms are:

- $b = 1$: the "simple" interpolating function, $\mu(x) = x/(1 + x)$
- $b = 2$: the "standard" interpolating $\mu(x) = x/\sqrt{1 + x^2}$

The two interpolation choices share limiting regimes but differ through the transition.

In both cases, $\mu(x) \to 1$ for $x \gg 1$ (Newtonian regime) and $\mu(x) \to x$ for $x \ll 1$ (deep MOND regime). It is to note that, the exact shape of the interpolating function is not fixed by first principle, but is instead chosen to satisfy the limiting behavior. Many studies have adopted the simple form ($b = 1$) (Famaey & Binney 2005; McGaugh 2011). The standard form ($b = 2$) is also used, as it was originally introduced by Milgrom (Milgrom 1983a; Sanders & McGaugh 2002). Beyond these, alternative interpolating functions have also been proposed to better match external-field constraints or

For 84 matched pairs, the median RV uncertainty improves by about 24 times.

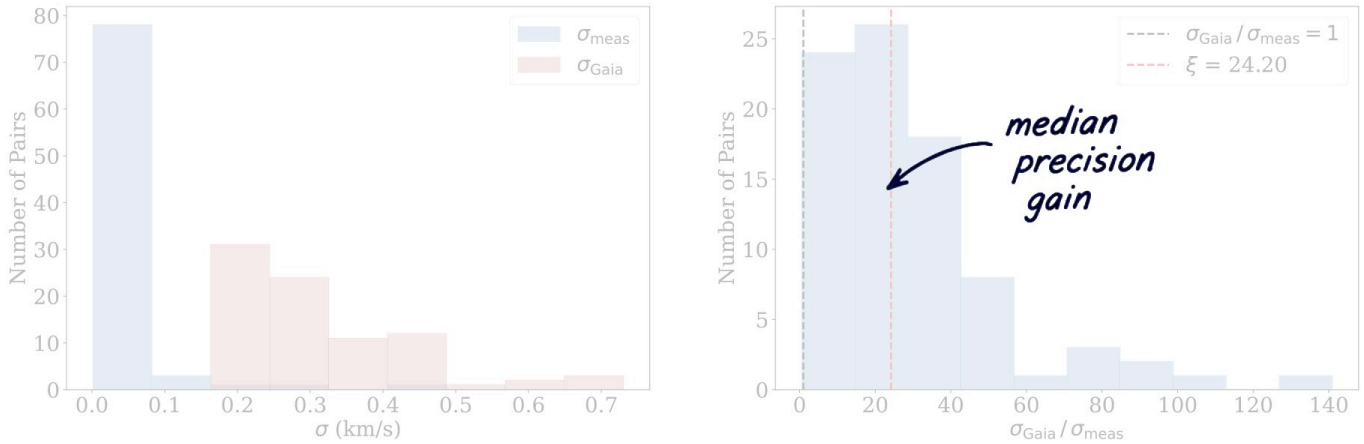


Figure 2. *Left:* Comparison of differential RV uncertainties between our measurements ($\sigma_{\rm meas}$, blue) and *Gaia* DR3 ($\sigma_{\rm Gaia}$, red) for 84 C3PO binary pairs with *Gaia* RVs available. Our uncertainties are concentrated at small values, while *Gaia* uncertainties are broadly distributed at much larger values. *Right:* Distribution of the ratio $\sigma_{\rm Gaia}/\sigma_{\rm meas}$. The median ratio is $\xi \approx 24$, meaning our measurements have median improvement of $\sim$24 times than *Gaia* DR3 RVs.

Table 1. Selected Binary Star Systems from VLT and Magellan Observations.

Instrument	Object A Gaia ID	Object B Gaia ID	$r_{\rm proj}$ (AU)	$\Delta\mu_{\alpha*}$ (mas yr^{-1})	$\Delta\mu_{\delta}$ (mas yr^{-1})	$\lvert\Delta$RV$\rvert$ (km s^{-1})	$\sigma_{\rm RV}$ (km s^{-1})
VLT	6274653310550270592	6274656261191532160	581	−1.84	−1.26	0.099	0.007
VLT	6193279279612173952	6193280031230266752	9546	1.13	−1.64	1.566	0.005
VLT	4837828175549438080	4837828179846041728	1276	0.37	1.60	0.816	0.016
...	...	...	...	...	...	...	...
Magellan	5798991008295120896	5798991008295109120	4885	0.96	1.01	0.279	0.015
Magellan	3616756294553180288	3616756294553180160	297	−0.61	3.85	1.229	0.014
Magellan	6369977876303556736	6369977773223661184	1667	−0.04	−0.16	0.085	0.005
...	...	...	...	...	...	...	...

Note. — The table represents a subset of C3PO binary pairs observed with VLT and Magellan instruments. Columns show the projected separation ($r_{\rm proj}$), proper motion differences in right ascension and declination ($\Delta\mu_{\alpha*}$, $\Delta\mu_{\delta}$), measured RV difference between components ($|\Delta$RV$|$), and RV measurement uncertainty ($\sigma_{\rm RV}$). The full table is available in the electronic version.

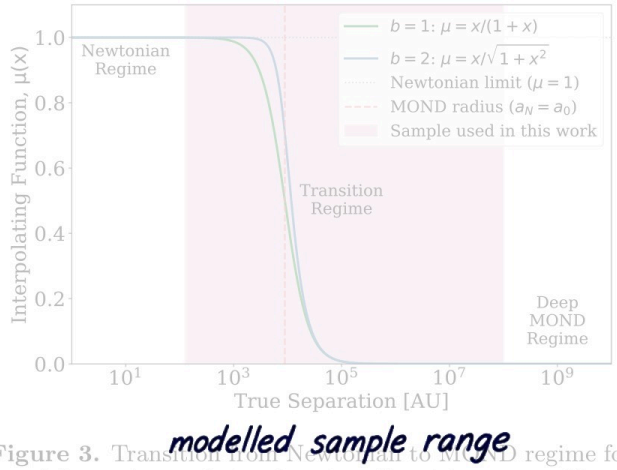


Figure 3. Transition from Newtonian to MOND regime for two different interpolating functions ($b = 1$ is green and $b = 2$ is blue). The pink shaded region indicates the range of true separation estimated by our model for the sample we used. The MOND radius ($a_N = a_0$) is marked with red dashed line and the Newtonian limit is marked as gray dotted lines. The transition is sharper for $b = 1$ than $b = 2$.

The comparison is a ratio of uncertainties for matched pairs, not a 24-fold gain in every gravity parameter.

specific galactic datasets (Zhao & Famaey 2006; Gentile et al. 2011). For our study, we chose both $b = 1$ and $b = 2$, and we compare our final results between them.

For wide binary systems like the C3PO sample, we must also account for the external gravitational field ($a_{\rm ext}$) from the galaxy. Unlike Newtonian gravity, where a uniform external field produces only tidal effects that are negligible for bound systems, in MOND, the external field modifies the internal dynamics even when spatially uniform. This is because the MOND acceleration depends on the total acceleration, not just the internal component. Because these systems are located in the solar neighborhood at galactocentric radius $R_{\rm GC} \approx 8$ kpc, where the galactic gravitational field produces $a_{\rm ext} \approx 2 \times 10^{-10}$ m s^{-2}, the external acceleration is comparable to a_0 and cannot be neglected. The total acceleration for each star depends on both the internal acceleration ($a_{\rm int}$) from the companion and the external acceleration ($a_{\rm ext}$) from the galaxy. The angle (θ) be-

The Galactic external field must enter the adopted low-acceleration model.

The adopted model combines orbital phase, orientation and the Galactic external field.

tween these vectors varies as the stars orbit each other. The magnitude of the total acceleration is,

The external field has a fixed adopted magnitude and direction toward the Galactic centre.

$$a_{\rm tot} = \sqrt{a_{\rm int}^2 + a_{\rm ext}^2 + 2a_{\rm int}a_{\rm ext}\cos\theta} \tag{4}$$

The effective acceleration in MOND is then,

$$a_{\rm eff} = \Big(\mu_{\rm tot}^2\, a_{\rm int}^2 + (\mu_{\rm tot} - \mu_{\rm ext})^2\, a_{\rm ext}^2 + 2\,\mu_{\rm tot}(\mu_{\rm tot} - \mu_{\rm ext})a_{\rm int}a_{\rm ext}\cos\theta\Big)^{1/2} \tag{5}$$

where $\mu_{\rm tot} = \mu(a_{\rm tot}/a_0)$ and $\mu_{\rm ext} = \mu(a_{\rm ext}/a_0)$.

For our calculations, we adopt an external acceleration value of $a_{\rm ext} = 2.1 \times 10^{-10}\ {\rm m\,s^{-2}}$ for the solar neighborhood, with the external field pointing toward the galactic center at $(\alpha_{\rm GC}, \delta_{\rm GC}) = (266.4051°, -28.936175°)$ (Desmond et al. 2024; Oort & Rougoor 1960).

3.2. *Orbital elements and Keplerian motion*

We describe each wide binary pairs with the six Keplerian orbital elements: semi-major axis a, eccentricity e, inclination i, longitude of ascending node Ω, argument of periastron ω, and mean anomaly M. The instantaneous separation between the two stars is,

$$r = \frac{a(1-e^2)}{1 + e\cos\nu} \tag{6}$$

where ν is the true anomaly obtained by solving Kepler's equation,

$$M = E - e\sin E \tag{7}$$

for the eccentric anomaly E, and then computing,

$$\nu = 2\tan^{-1}\Big(\sqrt{(1+e)/(1-e)}\,\tan[E/2]\Big) \tag{8}$$

We solve the Kepler's equation using the Newton-Raphson's method with 7 iterations. This precision is sufficient for our MOND analysis.

3.3. *MOND-modified velocities*

The key difference between MOND and Newtonian dynamics lies in the orbital velocity. In Newtonian mechanics, the velocity magnitude can be determined by using $a_N = G(M_1 + M_2)/r^2$. In MOND, we replace this with the effective acceleration $a_{\rm eff}$ from Equation 5. The orbital velocity magnitude becomes,

$$v = \sqrt{a_{\rm eff}\cdot r \cdot F} \tag{9}$$

where $F = (1 + e^2 + 2e\cos\nu)/(1 + e\cos\nu)$ accounts for velocity variations with orbital phase in an eccentric orbit. This velocity can be decomposed into tangential and radial components in the orbital plane:

The gravity inference is conditional on this external-field treatment.

$$v_r = -v\frac{e\sin\nu}{\sqrt{1 + e^2 + 2e\cos\nu}} \tag{10}$$

$$v_t = v\frac{1 + e\cos\nu}{\sqrt{1 + e^2 + 2e\cos\nu}} \tag{11}$$

For each star in the binary system, the velocities in Cartesian orbital coordinates are,

$$\vec{v}_{1,\rm orb} = \frac{M_2}{M_1 + M_2}\begin{pmatrix} v_r\cos\nu - v_t\sin\nu \\ v_r\sin\nu + v_t\cos\nu \\ 0\end{pmatrix} \tag{12}$$

$$\vec{v}_{2,\rm orb} = -\frac{M_1}{M_1 + M_2}\begin{pmatrix} v_r\cos\nu - v_t\sin\nu \\ v_r\sin\nu + v_t\cos\nu \\ 0\end{pmatrix} \tag{13}$$

3.4. *Coordinate transformation*

To convert orbital velocities to observed velocity components, we transform the coordinate from the orbital plane to International Celestial Reference System (ICRS). The rotation matrix is,

$$\mathcal{R} = \mathcal{R}_z(\Omega)\cdot\mathcal{R}_x(i)\cdot\mathcal{R}_z(\omega), \tag{14}$$

where $\mathcal{R}_z$ and $\mathcal{R}_x$ are rotation matrices about the z and x axes, respectively. The position and velocity vectors in ICRS coordinates are then,

Rotating the orbital vectors connects this geometric prescription to sky observables.

$$\vec{r}_{\rm ICRS} = \mathcal{R}\vec{r}_{\rm orb} \tag{15}$$

$$\vec{v}_{i,\rm ICRS} = \mathcal{R}\vec{v}_{i,\rm orb}, \quad i \in \{1, 2\} \tag{16}$$

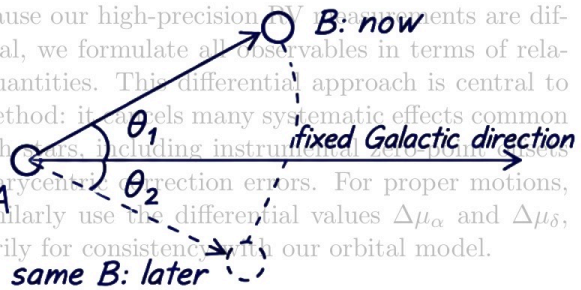
The angle θ in the Equation 5 is computed as,

$$\cos\theta = \hat{r}_{\rm ICRS}\cdot\hat{a}_{\rm ext} \tag{17}$$

where $\hat{r}_{\rm ICRS}$ is the unit vector pointing from star A to star B, and $\hat{a}_{\rm ext}$ points toward the Galactic center. This angle varies throughout the orbit, creating time-dependent modifications to the dynamics.

3.5. *Observable quantities*

Because our high-precision RV measurements are differential, we formulate all observables in terms of relative quantities. This differential approach is central to our method: it cancels many systematic effects common to both stars, including instrumental zero-point offsets and barycentric correction errors. For proper motions, we similarly use the differential values $\Delta\mu_\alpha$ and $\Delta\mu_\delta$, primarily for consistency with our orbital model.



- *Projected Separation*: For each star in a system, we define a local celestial coordinate system with unit

The inference shares one acceleration scale across all systems while fitting each orbit.

vectors $\hat{r}$ (radial), $\hat{e}$ (east), and $\hat{n}$ (north) based on the star's right ascension α and declination δ:

$$\hat{r} = (\cos\delta\cos\alpha, \cos\delta\sin\alpha, \sin\delta) \tag{18}$$
$$\hat{e} = (-\sin\alpha, \cos\alpha, 0) \tag{19}$$
$$\hat{n} = (-\sin\delta\cos\alpha, -\sin\delta\sin\alpha, \cos\delta) \tag{20}$$

The projected separation on the sky computed using the coordinates of star A is,

$$s_{\rm proj} = \sqrt{r_E^2 + r_N^2} \tag{21}$$

where $r_E = \vec{r}_{\rm ICRS} \cdot \hat{e}_A$ and $r_N = \vec{r}_{\rm ICRS} \cdot \hat{n}_A$.

- *Differential Radial Velocity*: Each binary system has a systematic velocity $\vec{v}_{\rm sys}$ common to both the components. The RV for each star is,

Relative observables still depend on viewing geometry and the system velocity.

$$v_{r,1} = (\vec{v}_{1,\rm ICRS} + \vec{v}_{\rm sys}) \cdot \hat{r}_A \tag{22}$$
$$v_{r,2} = (\vec{v}_{2,\rm ICRS} + \vec{v}_{\rm sys}) \cdot \hat{r}_B \tag{23}$$

The differential RV is,

$$\Delta v_r = v_{r,2} - v_{r,1} \tag{24}$$

- *Differential Proper Motion*: The tangential velocity components are,

$$\vec{v}_{i,t} = \vec{v}_{i,\rm ICRS} + \vec{v}_{\rm sys} - [(\vec{v}_{i,\rm ICRS} + \vec{v}_{\rm sys}) \cdot \hat{r}_i]\hat{r}_i \tag{25}$$

where $i \in \{1, 2\}$. The proper motions are,

$$\mu_{\alpha,i} = -\frac{\vec{v}_{i,t} \cdot \hat{e}_i}{4.74047 \times d_i} \tag{26}$$
$$\mu_{\delta,i} = \frac{\vec{v}_{i,t} \cdot \hat{n}_i}{4.74047 \times d_i} \tag{27}$$

where d_i is the distance in parsecs and the factor 4.74047 converts $\mathrm{km\,s^{-1}\,pc^{-1}}$ to mas $\mathrm{yr^{-1}}$. The differential proper motions are,

$$\Delta\mu_\alpha = \mu_{\alpha,2} - \mu_{\alpha,1} \tag{28}$$
$$\Delta\mu_\delta = \mu_{\delta,2} - \mu_{\delta,1} \tag{29}$$

Figure 4 illustrates the relative orbit in both three-dimensional view (in left) and projection onto the orbital plane (in right), with the key orbital elements indicated.

4. MODEL & INFERENCES

After defining the MOND orbital dynamics and geometry, we constructed a hierarchical Bayesian model to infer the MOND parameter a_0 and the orbital parameters for all 100 binary systems. Previous studies relying on ensemble statistics of Gaia proper motions have reached differing conclusions, possibly due to variations in sample selection and statistical methodology (Hernandez et al. 2024a). This motivated us to construct a hierarchical Bayesian framework that simultaneously models individual orbital elements and the global MOND parameter a_0, propagating uncertainties and accounting for degeneracies between parameters. The graphical structure of the model is shown in Figure 5. All priors and likelihoods are summarized in Table 2.

4.1. *Prior distribution*

We chose weakly informative priors that reflect physical constraints and existing knowledge while allowing the data to dominate the posterior. Below we describe and justify each prior choice:

- a_0 : A global MOND parameter a_0 that applies for all 100 wide-binary pairs. We place a uniform prior on $\log_{10} a_0$ spanning from -12 to -8. We chose this range so that the canonical MOND value of $\log_{10} a_0 \approx -9.92$ sits in the mid-range of the uniform prior and we can allow for similar weights on both Newtonian and MOND regimes. Going above -8 will not be physical as we do not expect to have such deep MOND regime. We also cannot have $a_0 < 0$ or $a_0 \approx 0$ in the prior because the MOND dynamics depend on the ratio $x = a_{\rm tot}/a_0$ when evaluating the interpolating function $\mu(x) = x/(1+x^b)^{(1/b)}$. If $a_0 \approx 0$ this ratio diverges, and the MOND acceleration becomes undefined. If $a_0 < 0$, the argument of $\mu(x)$ becomes negative which produces non-physical accelerations and complex-valued velocities in Equations 5 and 9. Such values cause the likelihood function to break numerically and violate the physical assumptions of MOND. We also verify the robustness of our results to alternative prior choices in Appendix C.

A finite prior in log acceleration excludes exact zero; Newtonian model comparison requires a separate calculation.

- M : Mass for each star in the binary pairs. As our sample consists of F, G, and K spectral type stars, we expect masses near 1 $\mathrm{M_\odot}$. We adopt Gaussian priors with mean 1.0 $\mathrm{M_\odot}$ and standard deviation 0.05 $\mathrm{M_\odot}$. This narrow range ensures $M_1 \neq M_2$, which is required to avoid singularities in Equations 12–13. However, the orbital dynamics depend primarily on the total mass $(M_1 + M_2)$ and the mass ratio $M_2/(M_1 + M_2)$. For our sample of similar-mass stellar pairs, this ratio remains close to 0.5. This makes our results insensitive to the precise mass values within physically reasonable ranges.

Orientation and orbital phase connect the true orbit to its projection on the sky.

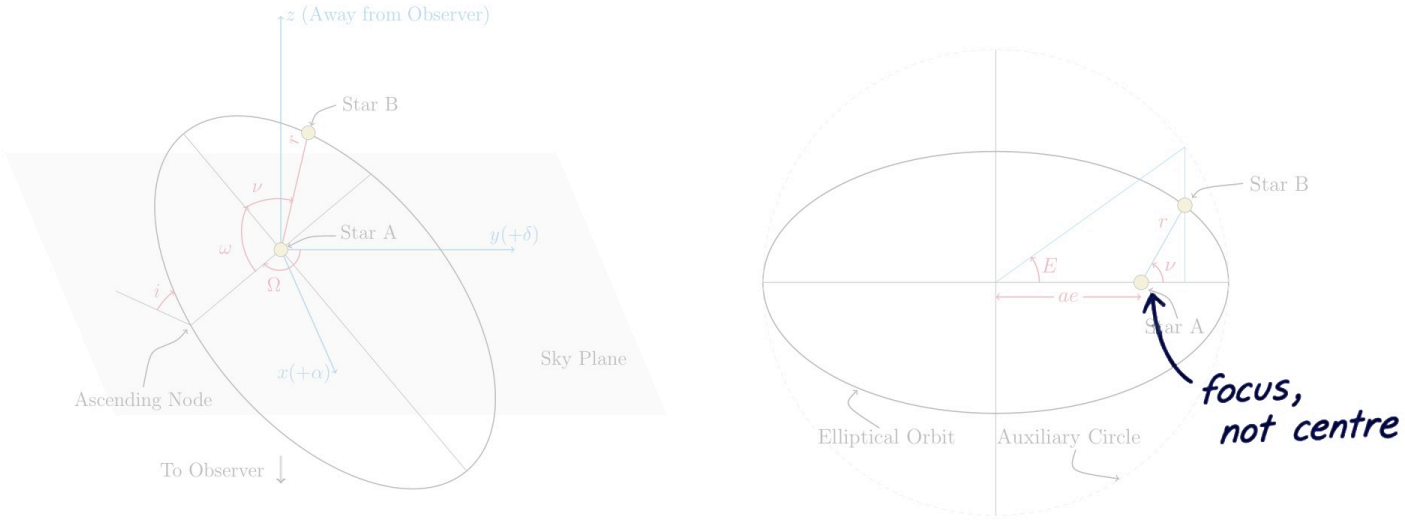


Figure 4. Relative orbits and Keplerian elements for wide binary systems. *Left:* Three-dimensional view showing the relative orbit of star B around star A (both yellow circles). The coordinate system is defined with the z-axis pointing away from the observer (RV direction), and x and y axes aligned with right ascension (α) and declination (δ). The orbital orientation is specified by inclination i (angle between orbital plane and sky plane), longitude of ascending node Ω (where the orbit crosses the sky plane moving away from the observer), argument of periastron ω (angle from ascending node to periastron), and true anomaly ν (angle from periastron to current position). The instantaneous separation between stars is r. *Right:* Orbital plane view of the same diagram showing the relationship between eccentric anomaly E, true anomaly ν, and the auxiliary circle. The distance ae represents the offset of the focus from the ellipse center, where a is the semi-major axis and e is the eccentricity.

- a : Semi-major axis of the relative orbit. We parameterize a, where $a_{\rm over}$ follows a log-normal prior with $\mu = 0.23 \times r_{\rm obs}$ and $\sigma = 0.5 \times r_{\rm obs}$. The choice 0.23 corresponds to a median scaling factor of $\exp(0.23) \approx 1.26$. This is consistent with expectations for randomly oriented orbits (Metchev & Hillenbrand 2009).

- e : Eccentricity of the relative orbit. Eccentricity distribution is important for wide-binary dynamics because orbital velocities depend strongly on eccentricity and orbital phase. High-eccentricity orbits spend most of their time near apastron with low velocities, so the observed velocity distribution is sensitive to the underlying eccentricity population. We therefore adopt a hierarchical, separation-dependent eccentricity distribution following Hwang et al. (2022b). Binaries are divided into five separation bins based on their projected separations: $[0, 100)$, $[100, 300)$, $[300, 1000)$, $[1000, 3000)$, and $[3000, 10^6)$ AU.

  For each bin k, we define a population-level shape parameter:

$$\alpha_k \sim \mathcal{N}(\mu_{\alpha,k}, \sigma^2_{\alpha,k}) \tag{30}$$

  where $\mu_\alpha = [-0.2, 0.4, 0.8, 1.0, 1.2]$ and $\sigma_\alpha = [0.3, 0.2, 0.2, 0.2, 0.2]$ for the five bins from the Hwang et al. (2022b). These hyperparameters reflect the expectation that wider-binaries have higher eccentricities on average. For a system j in bin k, the eccentricity is drawn from,

$$e_j \sim \mathrm{Beta}(\alpha'_k, 1) \tag{31}$$

  and truncated at $e_j < 0.98$ to avoid numerical instabilities near parabolic orbits. For this, we note that most wide binaries have extremely eccentric orbit (Hwang et al. 2022a). This prior is chosen based on observational evidences (Hwang et al. 2022b). We verified that our results are not sensitive to this choice by re-running the analysis with a uniform eccentricity prior: the posterior on a_0 shifted by less than 0.2 dex.

- i : Inclination of the relative orbit. We defined a uniform prior on $\cos i$ to produce an isotropic distribution for inclinations.

- ω : Argument of pericenter of the relative orbit. We defined ω to be uniform between 0 and 2π.

- Ω : Longitude of ascending node of the relative orbit. We defined Ω to be uniform between 0 and 2π.

- ϕ : Mean anomaly of the relative orbit. We defined ϕ to be uniform between 0 and 2π.

The eccentricity population varies with separation, with sensitivity checks against a uniform alternative.

Uniform cosine of inclination gives isotropic orientations; a uniform inclination would not.

One shared gravity parameter links 100 separate orbital models.

shared across pairs

The plate repeats the per-pair geometry and nuisance parameters; it does not create 100 independent estimates of the global scale.

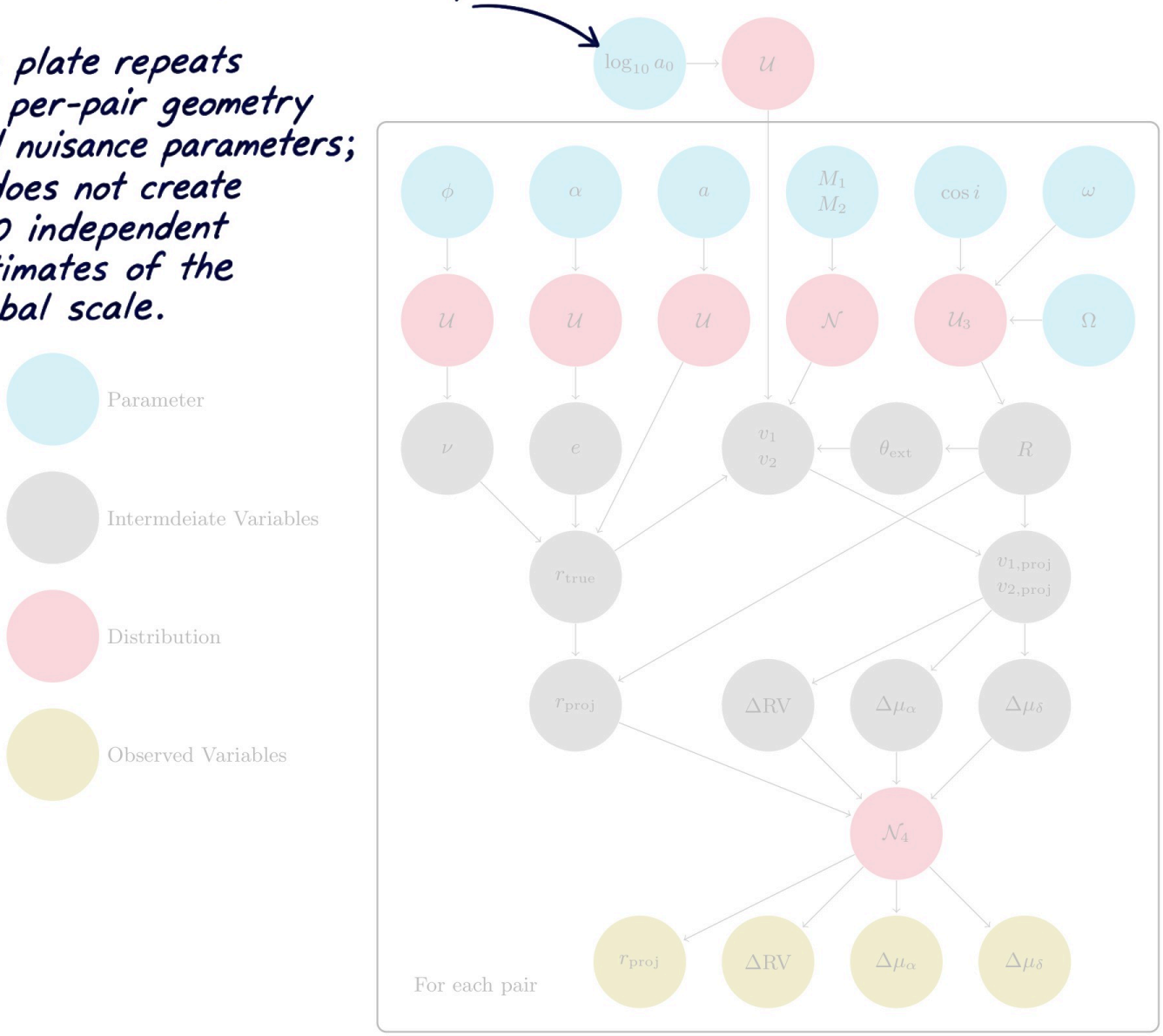


Figure 5. Graphical representation of the hierarchical Bayesian model for inferring MOND parameter a_0 and orbital elements. The global MOND acceleration scale $\log_{10} a_0$ (blue) is shared across all binary systems and inferred jointly from the full dataset. The box denotes plate notation, indicating that the enclosed structure is replicated for each of the $N = 100$ binary systems. For each system, we infer six orbital elements: semi-major axis a, eccentricity shape parameter α (which determines e via a Beta distribution), mean anomaly ϕ, inclination i, argument of periastron ω, and longitude of ascending node Ω, along with stellar masses M_1 and M_2. These parameters determine intermediate quantities (gray): true anomaly ν, instantaneous separation $r_{\rm true}$, external field angle $\theta_{\rm ext}$, rotation matrix R, and stellar velocities v_1, v_2. The model predicts four observables (yellow): projected separation $r_\perp$, differential radial velocity Δv_r, and differential proper motions $\Delta\mu_\alpha$ and $\Delta\mu_\delta$. Red nodes indicate probability distributions linking parameters to intermediate quantities or observations. N_4 denotes a 4-dimensional Gaussian likelihood over the observables. This model structure applies to both interpolating functions tested: $b = 1$ (simple) and $b = 2$ (standard), where b controls the sharpness of the transition between Newtonian and MOND regimes in Equation 3.

Projected separation, RV difference and two proper-motion differences supply the four constraints.

Priors, geometry and measurement errors together define the statistical model.

Table 2. Prior and likelihood distributions used for MOND analysis.

Parameter	Definition	Description
	Priors	
$\log_{10} a_0$	$\mathcal{U}(-13,-7)$, $\mathcal{U}(-12,-8)$, and $\mathcal{U}(-11,-9)$	Global MOND acceleration scale in log-space
$M_{i,j}$ ($M_\odot$)	$\mathcal{N}(1.0, 0.05^2)$	Stellar masses for each system
a_j (AU)	$\mathcal{N}(\ln(0.23 \cdot r_{\rm obs}), (0.5 \cdot r_{\rm obs})^2)$	Semi-major axis
α_k	$\mathcal{N}(\mu_{\alpha,k}, \sigma^2_{\alpha,k})$	Eccentricity shape parameter per bin
$\cos i_j$	$\mathcal{U}(-1,1)$	Inclination
ω_j	$\mathcal{U}(0,2\pi)$	Argument of periastron
Ω_j	$\mathcal{U}(0,2\pi)$	Longitude of ascending node
ϕ_j	$\mathcal{U}(0,2\pi)$	Mean anomaly
	Intermediate Variables	
e_j	Eq. 31	Eccentricity (from shape parameter)
E_j	Eq. 7	Eccentric anomaly
ν_j	Eq. 8	True anomaly
$r_{{\rm true},j}$	Eq. 6	Instantaneous separation
R_j	Eq. 14	Rotation matrix
$\theta_{{\rm ext},j}$	Eq. 17	External field angle
$v_{1,j}, v_{2,j}$	Eqs. 12–13	Stellar velocities (orbital frame)
$v_{1,{\rm proj},j}, v_{2,{\rm proj},j}$	Eq. 16	Projected stellar velocities (ICRS)
$r_{{\rm proj},j}$	Eq. 21	Model projected separation
$\Delta v_{r,{\rm model},j}$	Eq. 24	Model differential RV
$\Delta\mu_{\alpha,{\rm model},j}$	Eq. 28	Model differential proper motion (RA)
$\Delta\mu_{\delta,{\rm model},j}$	Eq. 29	Model differential proper motion (Dec)
	Likelihoods	
$s_{{\rm obs},j}$	$\mathcal{N}(s_{{\rm proj},j}, \sigma^2_{s,j})$	Projected separation
$\Delta v_{r,{\rm obs},j}$	$\mathcal{N}(\Delta v_{r,{\rm model},j}, \sigma^2_{\Delta v_r,j})$	Differential radial velocity
$\Delta\mu_{\alpha,{\rm obs},j}$	$\mathcal{N}(\Delta\mu_{\alpha,{\rm model},j}, \sigma^2_{\mu,j})$	Differential proper motion in Right Ascension
$\Delta\mu_{\delta,{\rm obs},j}$	$\mathcal{N}(\Delta\mu_{\delta,{\rm model},j}, \sigma^2_{\mu,j})$	Differential proper motion in Declination

Note. — Prior and likelihood distributions for the hierarchical Bayesian model. The global MOND parameter a_0 applies to all binary systems. For each system j, we infer all the other parameters. The eccentricity distribution depends on separation-dependent shape parameters α_k for different projected separation bins following Hwang et al. (2022b). Separation uncertainty $\sigma_{s,j}$ includes a 5% floor; $\sigma_{\Delta v_r,j}$ is from our differential RV analysis; $\sigma_{\mu,j}$ is from *Gaia*. We treat the *Gaia* proper motion measurements of the two stars as independent, which is appropriate given their wide angular separations.

The separation likelihood includes a 5% uncertainty floor for effects beyond formal parallax errors.

The proper-motion errors use an independence approximation for the two stars.

Converged sampling and residual checks support the fit, while gravity claims remain model-dependent.

4.2. *Likelihood functions*

We combine constraints from the observed projected separations, differential RV, and the differential proper motion.

- Projected Separation: The observed projected separation for system j is modeled as,

$$s_{\rm obs,j} \sim \mathcal{N}(s_{\rm proj,j}, \sigma^2_{s,j}) \tag{32}$$

  where $\sigma_{s,j}$ is derived from *Gaia* parallax uncertainties with a minimum floor of 5% of the observed separation to account for potential systematic uncertainties in the projection geometry and unmodeled astrometric correlations.

- Differential Radial Velocity: We model the differential RVs as following:

$$\Delta v_{r,\rm obs,j} \sim \mathcal{N}(\Delta v_{r,\rm model,j}, \sigma^2_{\Delta v_r,j}) \tag{33}$$

  where $\sigma_{\Delta v_r,j}$ is the measurement uncertainty from our differential RV analysis, obtained through bootstrap resampling of the per-order median as described in Section 2.

- Differential Proper Motion: The proper motion components are modeled as,

$$\Delta\mu_{\alpha,\rm obs,j} \sim \mathcal{N}(\Delta\mu_{\alpha,\rm obs,j}, \sigma^2_{\mu,j}) \tag{34}$$

$$\Delta\mu_{\delta,\rm obs,j} \sim \mathcal{N}(\Delta\mu_{\delta,\rm obs,j}, \sigma^2_{\mu,j}) \tag{35}$$

  where $\sigma_{\mu,j}$ is the *Gaia* proper motion uncertainty.

4.3. *Inference with HMC*

We performed Bayesian inference using Hamiltonian Monte Carlo (HMC) using the No-U-Turn Sampler (NUTS) (Hoffman et al. 2014). We implemented this using PyMC (Salvatier et al. 2015). HMC uses gradient information to explore high-dimensional parameter spaces, making it well-suited for our model with thousands of parameters including orbital elements for all 100 binary systems and population-level hyperparameters.

The NUTS algorithm automatically tunes the step size and number of leapfrog steps during an initial tuning phase by adapting to the local geometry of the posterior distribution. We ran 4 independent Markov chains, each with 2000 tuning steps and 3000 sampling steps, which produced a total of 12000 posterior samples. We set the target acceptance probability to 0.95 and the maximum tree depth to 10. This acceptance probability is standard for NUTS when dealing with correlated posteriors. Unlike traditional Metropolis-Hastings samplers where high acceptance rates can indicate poor mixing, NUTS automatically adapts its trajectory length based on the local posterior geometry. The higher target acceptance probability reduces the step size, which helps navigate the strong degeneracies between orbital parameters like semi-major axis a, eccentricity e, and orbital phase ϕ without overshooting.

Table 3. Posterior constraints on $\log_{10} a_0$

b	Median	Posterior CDF at Canonical a_0	Equivalent Gaussian Exclusion
1	−11.32	99.8%	3.1σ
2	−10.97	94.5%	1.9σ

weaker tension

NOTE— Posterior constraints on $\log_{10} a_0$ for the two interpolating functions using the uniform prior $\mathcal{U}(-12, -8)$. Results for alternative prior choices are presented in Appendix C.

4.4. *Model Diagnostics*

We used multiple diagnostics to assess convergence. The primary method was the Gelman-Rubin statistic $\hat{R}$ (Gelman & Rubin 1992), which compares the between-chain and within-chain variances. Convergence of a model. For our study, we required $\hat{R} < 1.01$ for all parameters to ensure that the chains had converged to the same distribution. In our final model, all parameters satisfied this requirement.

The residual width of about 1.1 leaves mild overdispersion beyond the nominal error model.

The reported 3.1 and 1.9 sigma tensions compare canonical acceleration with two different interpolation models.

We also examined the distribution of residuals to identify potential model misspecification or outliers. For the differential RV likelihood, we calculated normalized residuals,

$$z_i = \frac{\Delta v_{r,\rm obs,i} - \Delta v_{r,\rm model,i}}{\sigma_{\Delta v_r,i}} \tag{36}$$

Under a well-specified model, these residuals should follow a standard normal distribution. We found that the residual distribution has mean ≈ 0 and standard deviation ≈ 1.1, corresponding to a reduced chi-square of $\chi^2_\nu \approx 1.2$. This indicates a good model fit with slight overdispersion that may reflect unmodeled systematics or intrinsic stellar variability.

Figure 6 shows a corner plot of the posterior for one representative binary pair for $b = 1$, showing the correlations between a_0, orbital elements, and observables. The posteriors show good convergence visually with no apparent trends or multi-modality. Additional corner plots for other systems and for $b = 2$ are provided in Appendix A.

4.5. *Posterior Analysis*

The primary output of our analysis is the posterior distribution on $\log_{10} a_0$ for different choices of interpolating

This corner plot shows one system within the joint fit to all 100 binaries.

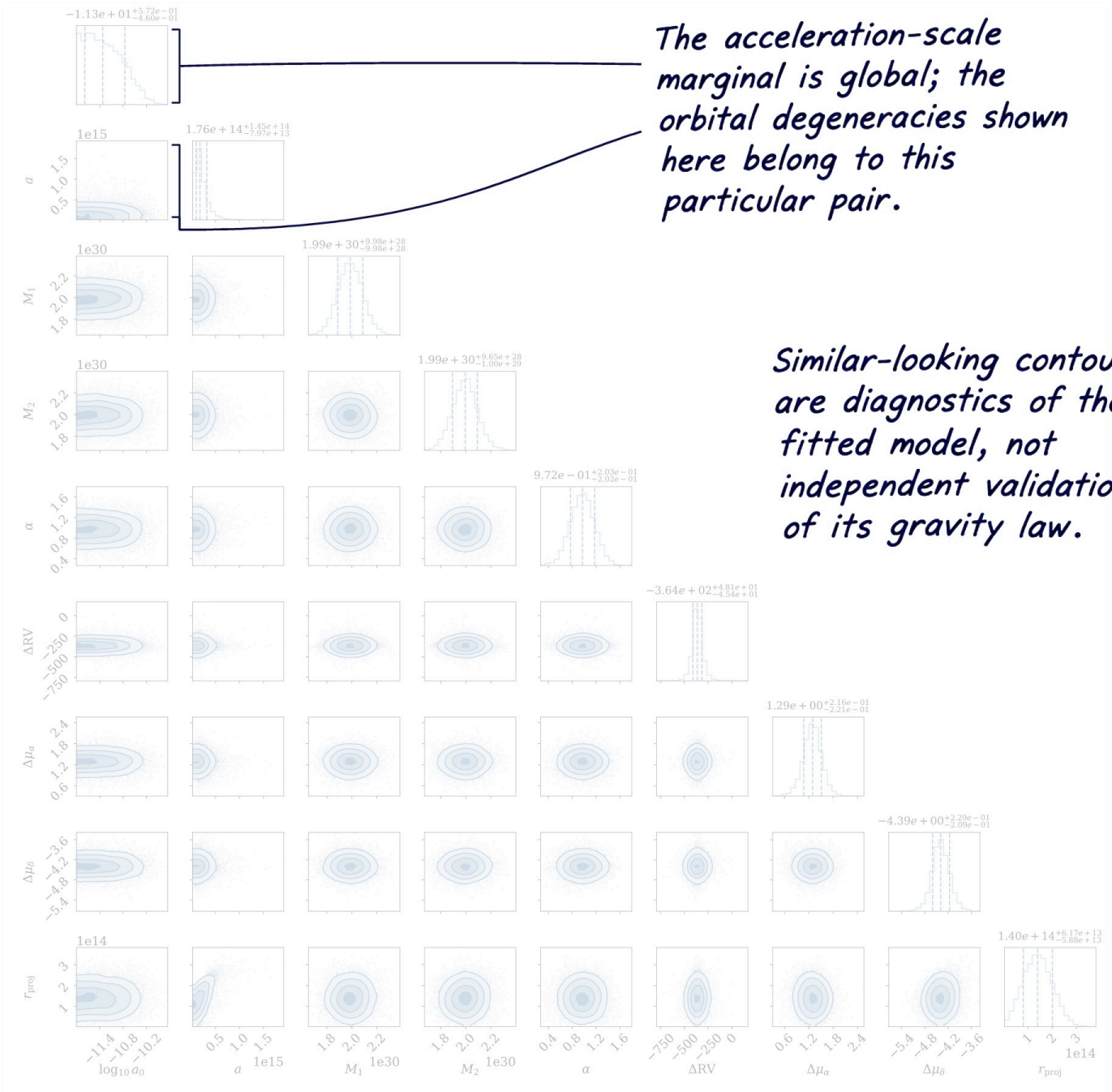


Figure 6. Corner plot showing the posterior distributions for one representative binary system, Gaia 6644929656684912512 and Gaia 6644929416166727680 considering $b = 1$. The parameters shown are: MOND acceleration scale in log-scale $\log_{10} a_0$, semi-major axis a, stellar masses M_1 and M_2, eccentricity distribution power α, model differential RV ΔRV, model differential proper motions $\Delta\mu_\alpha$ and $\Delta\mu_\delta$, and model projected separation $r_{\rm proj}$. We note that, though this figure shows the posterior for a single system, the inference was performed jointly across all 100 systems, with $\log_{10} a_0$ shared globally. The correlations shown here reflect the degeneracies for this particular system marginalized over the full joint posterior.

The inferred acceleration scale shifts when the interpolation function changes.

Blue b=2 retains more probability at higher acceleration than green b=1.

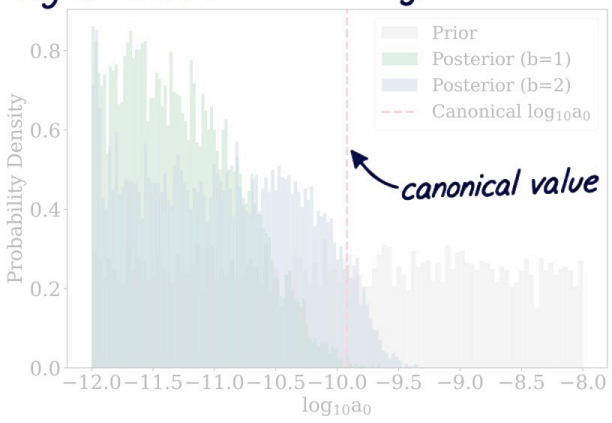


Figure 7. Comparison of posterior distributions for $\log_{10} a_0$ using the simple ($b = 1$, green) and standard ($b = 2$, blue) interpolating functions. The gray histogram shows the uniform prior $\mathcal{U}(-12, -8)$. The vertical dashed red line marks the canonical MOND value $\log_{10} a_0 = -9.92$. The $b = 2$ posterior is shifted toward higher a_0 values, indicating that constraints on a_0 depend on the assumed form of the interpolating function.

functions. We ran our hierarchical model with two fixed values of the sharpness parameter: $b = 1$ (simple interpolating function) and $b = 2$ (standard interpolating function). Figure 7 shows the posterior distributions for both interpolating functions using our fiducial uniform prior $\mathcal{U}(-12, -8)$.

Table 3 summarizes our constraints on a_0 for both interpolating functions. For $b = 1$, the posterior has a median of $\log_{10} a_0 = -11.32$ with a 68% credible interval of $[-11.78, -10.75]$. The canonical MOND value of $\log_{10} a_0 = -9.92$ lies at the 99.8th percentile of the posterior distribution, corresponding to exclusion at 3.1σ. This represents tension with MOND at the accepted a_0 value when using the simple interpolating function.

For $b = 2$, the posterior is broader and shifted toward higher values of a_0, with a median of $\log_{10} a_0 = -10.97$ and a 68% credible interval of $[-11.71, -10.22]$. The canonical MOND value lies at the 94.5th percentile, corresponding to exclusion at 1.9σ. This represents tension with MOND when using the standard interpolating function.

Figure 3 compares the two interpolating functions and how they change throughout different separations between the two components of a binary pair. It shows that the predicted true separation for our sample lies in the transition regime between Newtonian and MOND. Figure 7 directly compares the two posteriors. The $b = 2$ posterior is systematically shifted toward higher a_0 values compared to $b = 1$. It shows that constraints on a_0 from wide-binary dynamics depend on the assumed form of the interpolating function.

We verify that these results are robust to the choice of prior in Appendix C, where we present results for two alternative prior ranges: $\mathcal{U}(-11, -9)$ (narrower) and $\mathcal{U}(-13, -7)$ (wider). The qualitative conclusions remain unchanged across all prior choices.

5. DISCUSSIONS

5.1. *Results & statistical power*

Our differential RV technique achieves per-order precisions of 20–40 $\mathrm{m\,s^{-1}}$, which when combined across ∼30–50 echelle orders yields final precisions of ∼8–15 $\mathrm{m\,s^{-1}}$ per binary pair. This is comparable to the stability of exoplanet RV spectrographs such as HARPS ($\sim 1\ \mathrm{m\,s^{-1}}$) and HIRES with iodine cells ($\sim 3\ \mathrm{m\,s^{-1}}$), but achieved without specialized calibration hardware. Our technique is applicable to stellar pairs with similar spectral types, where one star serves as a spectral template for the other. This enables echelle-order-by-order comparison that cancels instrumental systematics.

Our sample of 100 binaries provides stronger constraints than studies using tens of thousands of *Gaia* wide binaries, which reflects the trade-off between sample size and measurement precision. Since Fisher information scales as σ^{-2}, our ∼24-fold precision improvement outweighs the smaller sample size. Beyond this, the measurement precision also determines which statistical approaches are viable. For *Gaia* RVs, the expected differential velocities of 50–200 $\mathrm{m\,s^{-1}}$ are smaller than typical uncertainties, meaning each system has signal-to-noise $\ll 1$. In this regime, individual orbital parameters are poorly constrained, so *Gaia*-based studies rely on ensemble statistics—comparing the aggregate distribution of observed velocities to forward-simulated predictions under different gravity models (El-Badry 2019). Our differential RV precision yields signal-to-noise $\approx$ 2–7 per system, which enables us to constrain individual orbits and perform hierarchical Bayesian inference that jointly fits orbital elements and the global parameter a_0. This approach can identify outliers and propagate orbital degeneracies into the final uncertainty on a_0.

The quoted tension is conditional on the adopted dynamics and finite log-acceleration prior.

Furthermore, as Fisher information scales as σ^{-2}, our 100 systems carry effective statistical weight equivalent to several $\times 10^4$ Gaia-quality systems. This is more than the total number of F, G, and K-type wide binaries available in *Gaia* at comparable separations (∼1,000–10,000 AU). Both of these reasons explain why our smaller sample has tighter constraints on a_0 than *Gaia*.

Our analysis yields posterior distributions for $\log_{10} a_0$ that depend on the assumed form of the MOND interpolating function. For $b = 1$, the canonical MOND value $a_0 = 1.2 \times 10^{-10}\ \mathrm{m\,s^{-2}}$ lies at the 99.8th percentile of

The result tests a specific dynamical prescription; external fields and hidden companions remain caveats.

the posterior, excluded at 3.1σ. For $b = 2$, the canonical value lies at the 94.5th percentile, excluded at 1.9σ.

5.2. *Interpretations*

Several interpretations of our results are possible which are described in the following:

- Our results could indicate that MOND, at least in its standard formulation, does not accurately predict the gravitational interaction between wide-binaries embedded in an external galactic field. This would not necessarily invalidate MOND's success in galactic scales if MOND is viewed as as an effective description rather than fundamental physics, but it would represent a limitation of the theory.

- The value $a_0 = 1.2 \times 10^{-10}$ m s^{-2} was determined primarily from rotation curves of spiral galaxies spanning 10–100 kpc with masses of 10^{10}–10^{12} $M_\odot$ (Begeman et al. 1991; McGaugh 2011; Famaey & McGaugh 2012). It is possible that a_0 depends on the physical environment, mass scale, or system type in ways not captured by the standard MOND framework. If the true uncertainty on a_0 is larger than commonly assumed, our measurements would be less discrepant than they appear. We note that our inference is conducted in $\log_{10}(a_0)$ space, which necessarily excludes $a_0 = 0$. This is appropriate for testing MOND, where $a_0 > 0$ by construction; a direct comparison with Newtonian gravity would require a separate model comparison framework. The tendency of the posterior to accumulate toward lower a_0 values is suggestive, and we have verified this trend is robust across different prior choices (Appendix C).

Exact Newtonian gravity is outside the finite log-acceleration prior used here.

- Our results shows sensitivity to the choice of interpolating function. The $b = 2$ posterior shows weaker tension with the canonical a_0 than $b = 1$. It is possible that the true interpolating function differs from both standard forms, or that additional parameters beyond a_0 and b are needed to describe MOND dynamics in external fields. We do not have enough data, but if we had, it would be possible to jointly fit b and a_0 to determine which interpolating functions are preferred by the observations.

- Our treatment of the external field effect assumes simple vector addition of internal and external accelerations, which may not fully capture the behavior in different MOND formulations. The precise behavior of MOND in external fields remains an area of active development, and relativistic extensions such as TeVeS may predict different behaviors (Bekenstein 2004b; Blanchet & Novak 2011; Sanders 2015; Chae et al. 2022). We also assumed a constant external field pointing toward the Galactic center with magnitude $a_{\rm ext} = 2.1 \times 10^{-10}$ m s^{-2}, but the true external field may include system-to-system variations due to local density fluctuations.

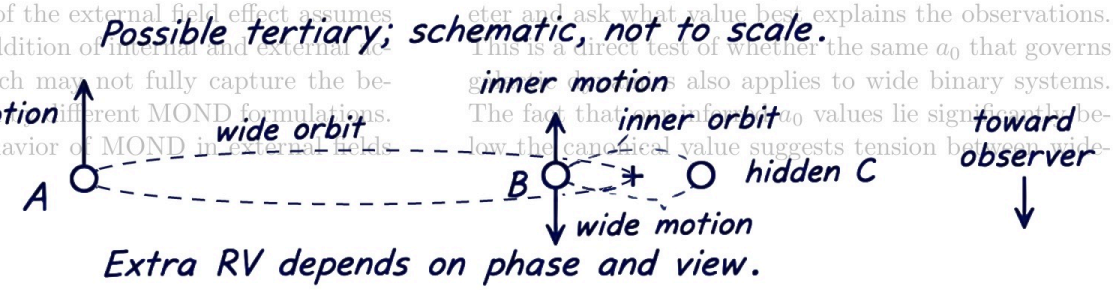
The assumed external field and unresolved tertiary companions can alter the interpretation.

- Some wide binary pairs in our sample could contain unresolved tertiary companions, which would introduce additional velocity components not captured by our two-body model. Although, the C3PO sample underwent visual inspection of spectra to exclude obvious double-lined spectroscopic binaries (SB2s) (Yong et al. 2023), and the consistency of our differential RVs with *Gaia* measurements suggests that tertiary contamination is not a dominant source of error. If unresolved triples are present, they could bias our inferred a_0, though the direction and magnitude of this bias depends on the specific configuration of each system.

5.3. *Comparison to previous studies*

Our approach differs from previous wide-binary MOND tests in many ways. Most importantly, we directly infer the MOND acceleration scale a_0 as a free parameter, rather than assuming its canonical value and testing for consistency. Previous wide-binary studies using *Gaia* data (Hernandez et al. 2022; Hernandez 2023; Hernandez et al. 2024b; Chae 2023, 2024a,b; Pittordis & Sutherland 2023; Banik et al. 2024) have adopted the canonical $a_0 = 1.2 \times 10^{-10}$ m s^{-2} from galaxy rotation curves and instead measured the effective gravity boost γ (where $G \to \gamma G$). These studies reported $\gamma = 1.43 \pm 0.06$ (Chae 2023), $\gamma = 1.49 \pm 0.2$ (Chae 2024a), and $\gamma = 1.5 \pm 0.2$ (Hernandez et al. 2024b), consistent with AQUAL predictions of $\gamma \approx 1.4$ for wide binaries in the solar neighborhood. In contrast, Banik et al. (2024) reported a 19σ preference for Newtonian gravity ($\gamma = 1$). As discussed in the review by Hernandez et al. (2024a), the conflicting conclusions came from differences in sample selection, treatment of hidden triple systems, and statistical methodology.

Our approach is more analogous to how a_0 was originally determined from galaxy rotation curves (Begeman et al. 1991; McGaugh 2011): we treat a_0 as a free parameter and ask what value best explains the observations. This is a direct test of whether the same a_0 that governs galaxy dynamics also applies to wide binary systems. The fact that our inferred a_0 values lie significantly below the canonical value suggests tension between wide-



Improved spectra help, but stellar offsets and population assumptions still set the interpretation.

binary kinematics and the MOND acceleration scale derived from galaxies.

Beyond this difference, our approach uses high-precision differential RVs and hierarchical Bayesian inference to model each binary system in three dimensions. Previous *Gaia*-based studies relied primarily on sky-projected (2D) relative velocities derived from proper motions, as *Gaia* RV uncertainties ($\sim$1000 $\mathrm{m\,s^{-1}}$) exceed the expected velocity differences in wide binaries. The most directly comparable work is Saglia et al. (2025), who used archival HARPS observations of 32 wide binaries to perform three-dimensional kinematic analysis with precise RVs. However, their study tested only Newtonian gravity without fitting for MOND parameters, measured absolute rather than differential RVs (increasing sensitivity to instrumental systematics and stellar convective shifts), and used a smaller sample.

5.4. *Methodological considerations*

5.4.1. *Data and measurements*

An improvement in getting more precise RV is to use full Bayesian forward modeling of each spectrum including instrumental line-spread functions, telluric contamination, and order-level jitter terms (Langford et al. 2025). While this could yield slightly tighter uncertainties, performing such fits for 200 stars individually is computationally expensive. Another direction of improvement is the easiest to guess: increasing the sample size by collecting more high resolution and high SNR data of wide-binaries. To verify that our conclusions are not driven by a few systems with unusually high precision, we repeated our analysis excluding high-precision outliers and find consistent results (Appendix B).

A potential concern for the RV measurement that we did is that stars with different surface gravities exhibit systematic RV offsets at the $\sim$100 $\mathrm{m\,s^{-1}}$ level due to convective blueshift (which varies with spectral type) and gravitational redshift (which scales as $GM/Rc \sim$ 100 $\mathrm{m\,s^{-1}}$ for solar-type stars, with differences of order 10% between stars of different $\log g$). However, for C3PO wide-binaries, most of these effects cancel because the C3PO binary components have similar stellar spectra. with very similar masses and radii, the spectral types (F, G, K dwarfs) were homogenized by the survey selection criteria, and both stars were observed with identical instrumental setups. Therefore, we expect $\log g$-dependent RV offsets to contribute at most a few $\mathrm{m\,s^{-1}}$, which is well below our measurement precision. But if we could use more precise RVs in the future, we also need to correct for this RV offset due to surface gravity.

Similar stellar spectra help cancel convective and gravitational shifts; remaining offsets matter as precision improves.

5.4.2. *Modeling*

The treatment of stellar masses in our study uses Gaussian priors centered at solar mass with standard deviation 0.05 $\mathrm{M_\odot}$. One potential improvement would be to use isochrones to estimate masses from photometric and spectroscopic parameters. However, current isochrones have systematic uncertainties at the level relevant for our analysis (Valle et al. 2013, 2014). We verified that widening the mass priors to ± 0.2 $\mathrm{M_\odot}$ shifts the posterior on a_0 by less than 0.15 dex, as the dynamics depend primarily on the total mass and mass ratio rather than individual masses.

Broader mass priors were tested, while a more realistic systemic-velocity model is a future refinement.

Also, the systemic velocities of the binary systems are currently modeled with independent Gaussian priors centered at zero for each of the three velocity components. These systemic velocities represent the center-of-mass motion of each binary through the Galaxy, which must be separated from the orbital velocities we use to constrain a_0. Our current approach is appropriate for the thin disk population that dominates our sample, but it does not exploit the fact that nearby stars exhibit kinematic structure related to the local standard of rest and known moving groups. Incorporating a kinematic model that accounts for the velocity distribution of the thin disk could help constrain the systemic velocities more tightly, reducing degeneracies with the orbital velocities.

Our prior on $\log_{10} a_0$ is uniform from -12 to -8. This range was chosen so that the canonical MOND value ($\log_{10} a_0 = -9.92$) lies near the middle to allow the data to favor either Newtonian-like behavior (lower a_0) or MOND-like behavior (higher a_0) with similar prior weights. As discussed in our formalism, the model requires a non-zero a_0. However, this also means that our conclusions depend on this prior choice, especially if the true value of a_0 is zero (and hence $\log_{10} a_0$ approaches negative infinity). We deem our choice of prior reasonable given the current formalism, but ultimately, the constraints suggest that the data would benefit from a larger sample size. While there are strong tentative suggestions that the posterior is concentrating toward the lower end of the allowed prior range, a larger sample would mitigate the current dependency on prior choice, and expanding the C3PO sample would be beneficial for this purpose. We present results for alternative prior choices in Appendix C.

A posterior near the lower prior boundary calls for explicit prior-sensitivity checks.

6. CONCLUSIONS

We present a test of MOND using high-precision differential RVs of 100 wide-binary pairs from the C3PO survey. Firstly, we developed a pixel-integrated spectral fitting technique for echelle spectroscopy that achieved

The reusable advance is precise differential spectroscopy joined to a shared orbital inference.

differential RV precisions of ∼8–15 $\mathrm{m\,s^{-1}}$ per binary pair, a factor of ∼24 improvement over *Gaia* RVs.

Secondly, we constructed a hierarchical Bayesian model that jointly infers the orbital elements of all 100 binary systems and the global MOND parameter a_0. Our three-dimensional orbital model accounts for the six Keplerian elements per system, stellar masses, the external galactic field, and systemic velocities along with marginalizing over all nuisance parameters. This approach propagates uncertainties from orbital degeneracies into the final constraints on a_0, and allows identification of individual system posteriors rather than relying on ensemble statistics only. The framework combines our differential RV measurements with *Gaia* astrometry (proper motions and projected separations) to constrain the three-dimensional kinematics of each binary pair.

We tested two widely used interpolating functions: the simple form ($b = 1$) and the standard form ($b = 2$). For $b = 1$, our posterior on $\log_{10} a_0$ has a median of -11.32, and the canonical MOND value $\log_{10} a_0 = -9.92$ lies at the 99.8th percentile, excluded at 3.1σ. For $b = 2$, the posterior has a median of -10.97 and the canonical value lies at the 94.5th percentile, excluded at 1.9σ. These results are robust to the choice of prior on a_0.

Our results indicate that C3PO wide binary kinematics show tension with MOND at the canonical a_0 value, with the degree of tension depending on the assumed interpolating function. This result suggests the importance of the interpolating function choice in MOND tests and suggests that constraints on a_0 from different astrophysical systems may not be directly comparable without accounting for this degeneracy.

The strength of the reported canonical-MOND tension depends on the interpolation choice.

Within the MOND framework, our findings suggest either that the canonical a_0 value does not apply universally across all astrophysical systems, that the interpolating function differs from standard forms, or that the external field effect in the solar neighborhood requires more robust treatment than current MOND formulations provide. The methodology we have developed can also be applied to future surveys to perform precise tests of gravity in the low-acceleration regime.

ACKNOWLEDGMENTS

We thank Kareem El-Badry for helpful discussion. We also appreciate the comments on precise RV measurements from Andrew Gould, Alex Ji, and Daniel Kelson throughout the past few months. We thank Fan Liu for helping curate the data as part of the C3PO program.

SMS is supported by the Distinguished University Fellowship awarded by The Ohio State University. YST is supported by NSF under Grant AST-2406729.

This work has made use of data from the European Space Agency (ESA) mission *Gaia* (https://www.cosmos.esa.int/gaia), processed by the *Gaia* Data Processing and Analysis Consortium (DPAC, https://www.cosmos.esa.int/web/gaia/dpac/consortium). Funding for the DPAC has been provided by national institutions, in particular the institutions participating in the *Gaia* Multilateral Agreement.

While the scientific content, draft and analysis are entirely from the authors, this project has benefited from collaboration with AI tools: Cursor for coding development and Claude-Opus-4.5 for proofreading of the final manuscript.

This work has also made use of the following software packages: AstroPy (Astropy Collaboration et al. 2013), PyMC (Salvatier et al. 2015), and ArviZ (Kumar et al. 2019).

APPENDIX

A. MODEL POSTERIORS

To demonstrate the consistency of our inference across different systems and interpolating functions, we include additional corner plots. Figure 8 shows the posterior for a second representative binary pair with b = 1. Figures 9 and 10 show the same two systems as Figures 6 and 8, but analyzed with b = 2.

B. ROBUSTNESS TO HIGH-PRECISION OUTLIERS

The appendix checks whether a few extreme precision-gain pairs dominate the result.

As noted in Section 2, pairs with the very high precision improvements contribute disproportionately to the statistical power as Fisher information scales as σ^{-2}. To verify that our conclusions are not driven by a few systems with high precision ratios, we repeated our full analysis after excluding pairs with $\sigma_{\mathrm{Gaia}}/\sigma_{\mathrm{meas}} > 60$. This removes the tail of the distribution shown in Figure 2 (right panel).

Table 4 shows the posterior constraints on $\log_{10} a_0$ for this restricted sample using the $\mathcal{U}(-12, -8)$ prior, and Figure 11 compares the posterior distributions. The results do not change significantly and the final outcome is the same: the canonical MOND value remains excluded at $\sim 3\sigma$ for $b = 1$ and $\sim 1.9\sigma$ for $b = 2$.

A second binary shows local orbital structure; the lower table tests sample robustness.

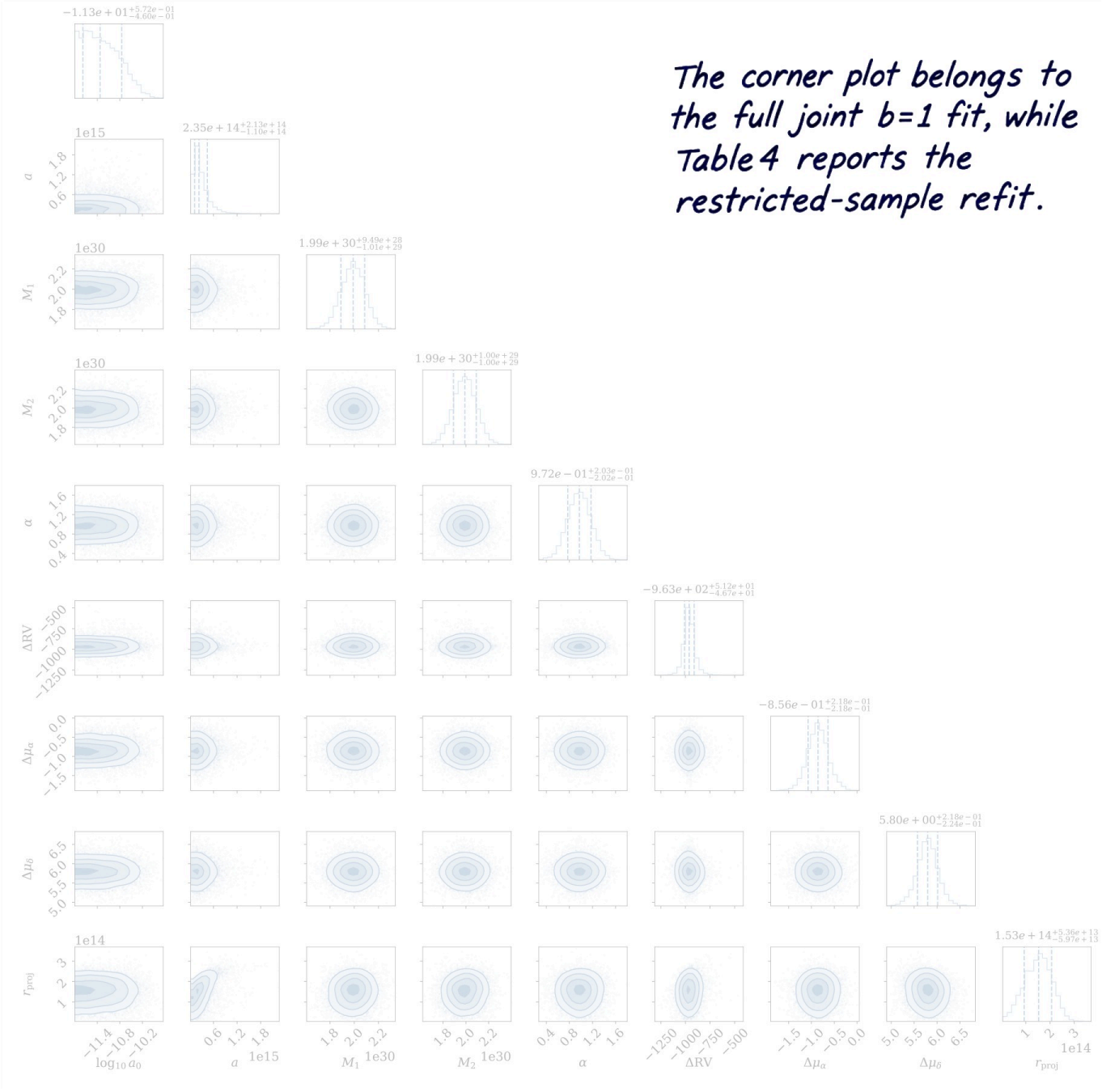


Figure 8. Same as Figure 6, for binary pair Gaia 2356080043380354816 and Gaia 2356290256259997696 with $b = 1$.

Table 4. Posterior constraints on $\log_{10} a_0$ for $\sigma_{\rm Gaia}/\sigma_{\rm meas} < 60$

b	Median	68% CI	Posterior CDF at Canonical a_0	Equivalent Gaussian Exclusion
1	-11.28	$[-11.74, -10.73]$	99.7%	3.0σ
2	-10.96	$[-11.67, -10.20]$	94.2%	1.9σ

NOTE— Same as Table 3 but excluding pairs with $\sigma_{\rm Gaia}/\sigma_{\rm meas} > 60$, using the $\mathcal{U}(-12, -8)$ prior.

Removing pairs with precision ratio above 60 leaves reported tensions near 3.0 and 1.9 sigma.

Changing to the standard interpolation changes the shared fit while retaining this pair's local parameters.

This is the same binary as Figure 6, now with $b = 2$; its global acceleration marginal comes from the joint sample.

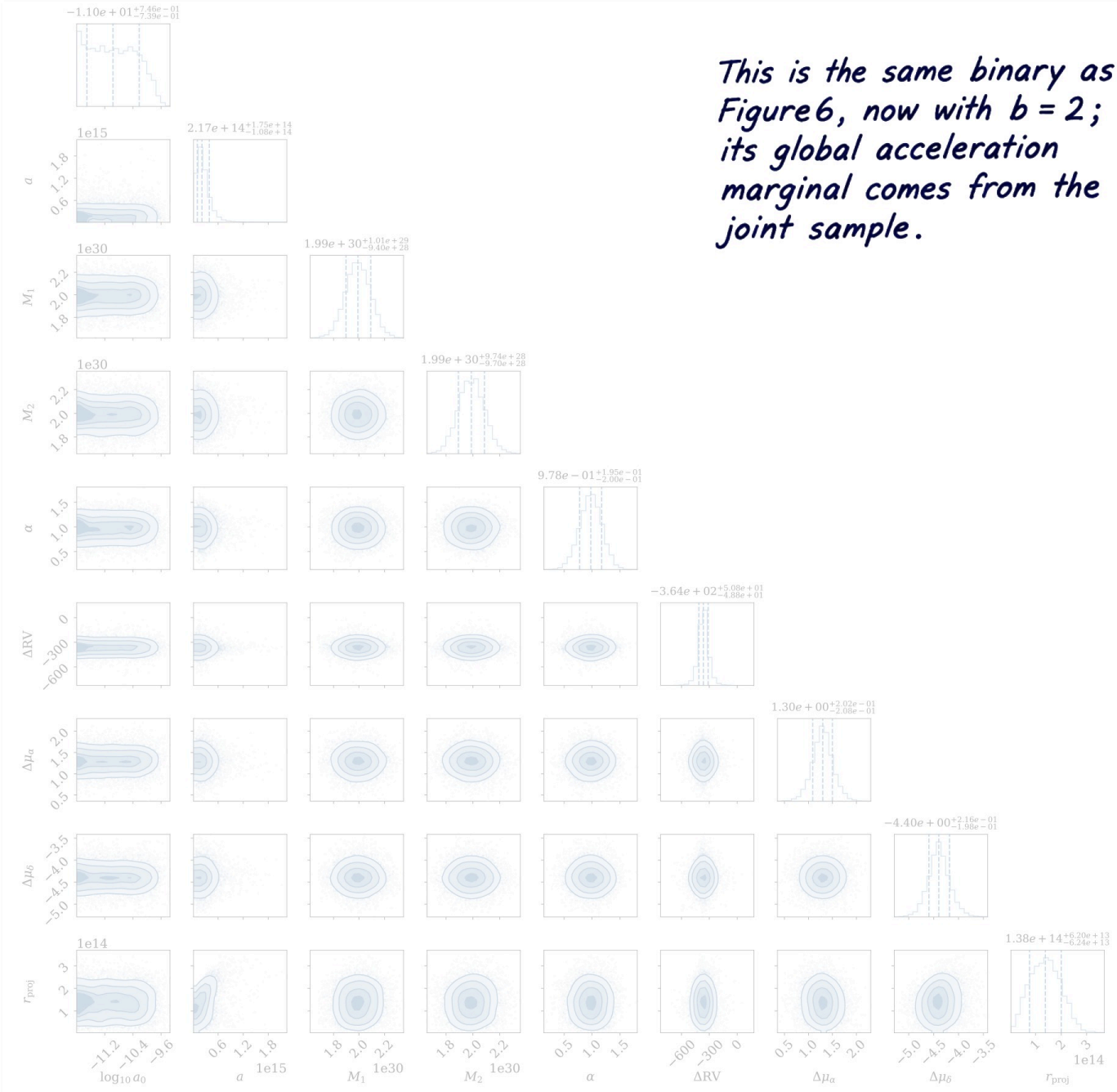


Figure 9. Same as Figure 6, for the same binary pair but for $b = 2$.

C. PRIOR SENSITIVITY ANALYSIS

The following prior checks test how much the allowed acceleration range shapes the inference.

To further verify the dependence of our results to the choice of prior on $\log_{10} a_0$, we repeated our analysis with two alternative prior ranges: a narrower prior $\mathcal{U}(-11, -9)$ and a wider prior $\mathcal{U}(-13, -7)$. Table 5 summarizes the results for all three prior choices, and Figure 12 shows the corresponding posterior distributions.

REFERENCES

Angus, G. W. 2008, MNRAS, 387, 1481, doi: 10.1111/j.1365-2966.2008.13351.x

Astropy Collaboration, Robitaille, T. P., Tollerud, E. J., et al. 2013, A&A, 558, A33, doi: 10.1051/0004-6361/201322068

The second pair is also shown under the standard interpolation.

Compare with Figure8 for the same pair under b = 1; read numerical axes rather than comparing contour widths by eye.

The global parameter is shared, but each binary retains its own velocity and geometry constraints.

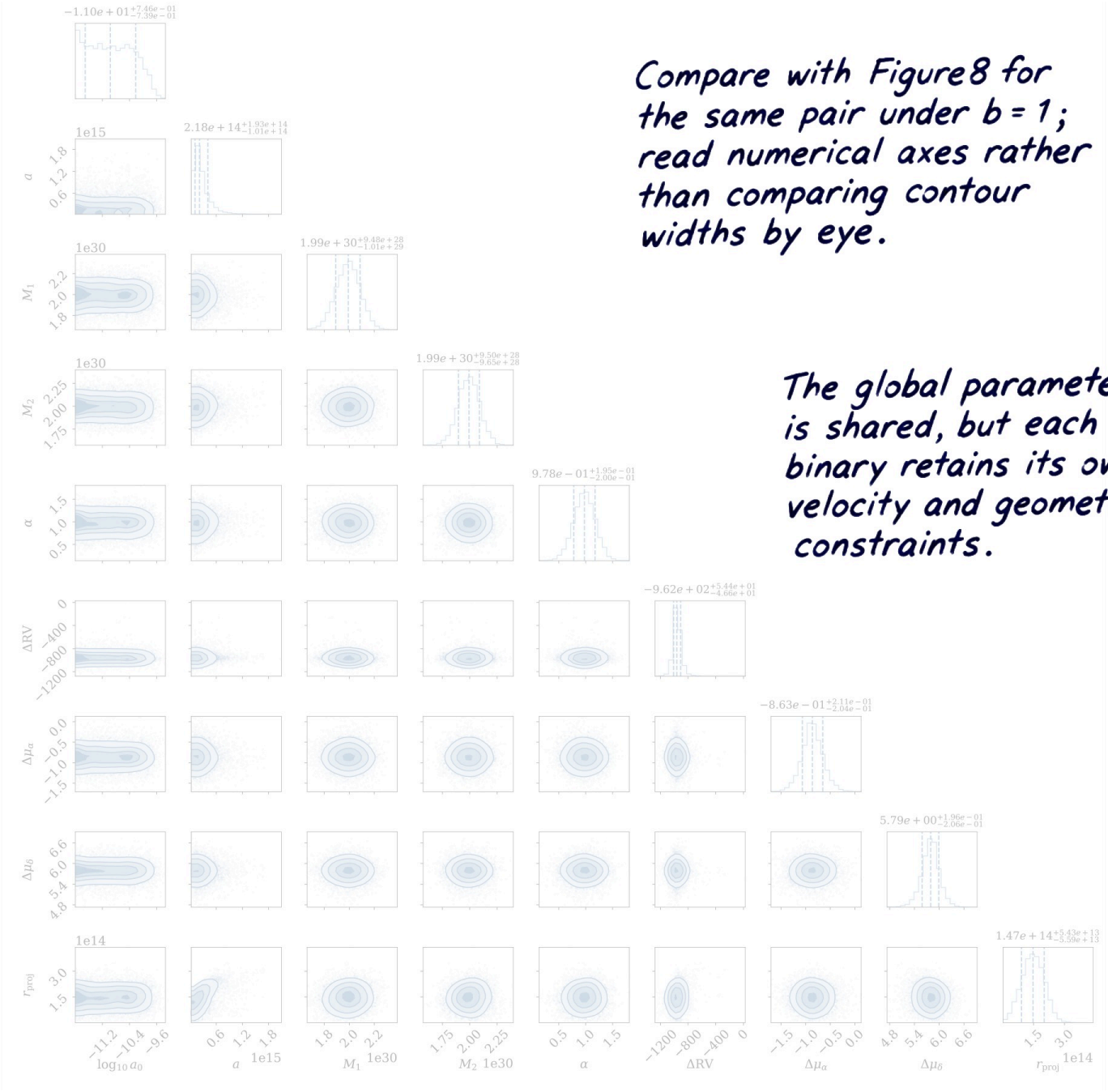


Figure 10. Same as Figure 8, for the same binary pair but for $b = 2$.

Banik, I., Pittordis, C., Sutherland, W., et al. 2024, MNRAS, 527, 4573, doi: 10.1093/mnras/stad3393

Banik, I., & Zhao, H. 2018, MNRAS, 480, 2660, doi: 10.1093/mnras/sty2007

Bedell, M., Bean, J. L., Meléndez, J., et al. 2018, ApJ, 865, 68, doi: 10.3847/1538-4357/aad908

Begeman, K. G. 1989, A&A, 223, 47

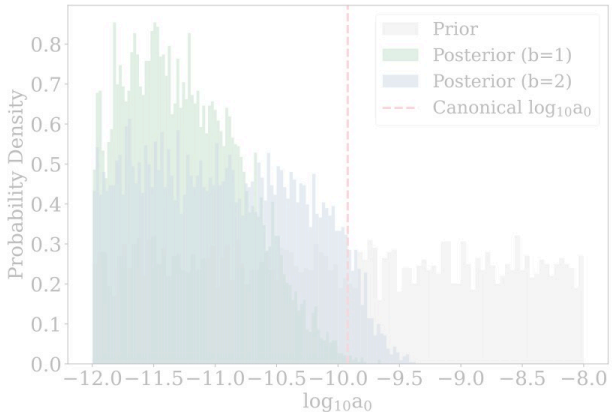
Begeman, K. G., Broeils, A. H., & Sanders, R. H. 1991, MNRAS, 249, 523, doi: 10.1093/mnras/249.3.523

Bekenstein, J., & Milgrom, M. 1984, ApJ, 286, 7, doi: 10.1086/162570

Bekenstein, J. D. 2004a, PhRvD, 70, 083509, doi: 10.1103/PhysRevD.70.083509

—. 2004b, PhRvD, 70, 083509, doi: 10.1103/PhysRevD.70.083509

The low-acceleration preference persists, but its location and quoted significance depend on the prior.



The upper plot removes the extreme precision-ratio pairs; it is a sample-selection check.

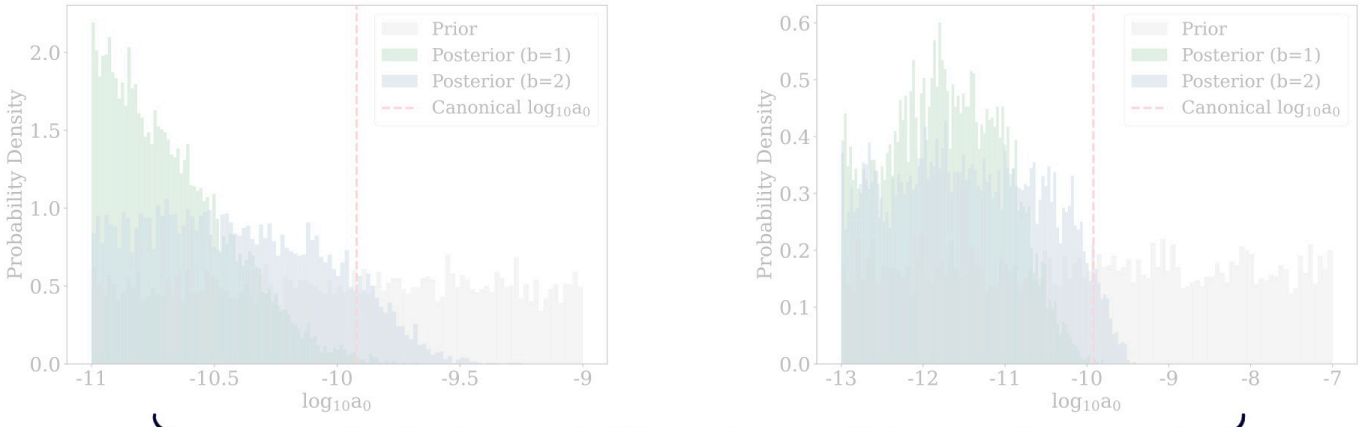
Figure 11. Same as Figure 7 but excluding pairs with $\sigma_{\rm Gaia}/\sigma_{\rm meas} > 60$.

Across tested priors, reported tension spans 2.8–3.4 sigma for b=1 and 1.6–2.1 sigma for b=2.

Table 5. Prior sensitivity analysis for $\log_{10} a_0$

b	Prior	Median	68% CI	Posterior CDF at Canonical a_0	Equivalent Gaussian Exclusion
1	$\mathcal{U}(-11,-9)$	-10.72	$[-10.92,-10.41]$	99.5%	2.8σ
	$\mathcal{U}(-12,-8)$	-11.32	$[-11.78,-10.75]$	99.8%	3.1σ
	$\mathcal{U}(-13,-7)$	-11.75	$[-12.53,-11.00]$	99.9%	3.4σ
2	$\mathcal{U}(-11,-9)$	-10.45	$[-10.82,-10.02]$	89.6%	1.6σ
	$\mathcal{U}(-12,-8)$	-10.97	$[-11.71,-10.22]$	94.5%	1.9σ
	$\mathcal{U}(-13,-7)$	-12.49	$[-12.49,-10.42]$	96.3%	2.1σ

NOTE— Posterior constraints on $\log_{10} a_0$ for different prior choices.



The lower two panels use different prior ranges and axis spans, so histogram heights are not directly comparable.

Figure 12. Posterior distributions for $\log_{10} a_0$ using alternative priors. *Left:* Narrower prior $\mathcal{U}(-11,-9)$. *Right:* Wider prior $\mathcal{U}(-13,-7)$. [illegible] the canonical MOND value $\log_{10} a_0 = -9$ [illegible]

Bernstein, R., Shectman, S. A., Gunnels, S. M., Mochnacki, S., & Athey, A. E. 2003, in Society of Photo-Optical Instrumentation Engineers (SPIE) Conference Series, Vol. 4841, Instrument Design and Performance for Optical/Infrared Ground-based Telescopes, ed. M. Iye & A. F. M. Moorwood, 1694–1704, doi: 10.1117/12.461502

Blanchet, L., & Novak, J. 2011, MNRAS, 412, 2530, doi: 10.1111/j.1365-2966.2010.18076.x

Bouchy, F., Pepe, F., & Queloz, D. 2001, A&A, 374, 733, doi: 10.1051/0004-6361:20010730

Bullock, J. S., & Boylan-Kolchin, M. 2017, ARA&A, 55, 343, doi: 10.1146/annurev-astro-091916-055313

Chae, K.-H. 2023, ApJ, 952, 128, doi: 10.3847/1538-4357/ace101
—. 2024a, ApJ, 972, 186, doi: 10.3847/1538-4357/ad61e9
—. 2024b, ApJ, 960, 114, doi: 10.3847/1538-4357/ad0ed5
Chae, K.-H., Lelli, F., Desmond, H., McGaugh, S. S., & Schombert, J. M. 2022, PhRvD, 106, 103025, doi: 10.1103/PhysRevD.106.103025
Desmond, H., Hees, A., & Famaey, B. 2024, MNRAS, 530, 1781, doi: 10.1093/mnras/stae955
Di Cintio, A., Brook, C. B., Macciò, A. V., et al. 2014, MNRAS, 437, 415, doi: 10.1093/mnras/stt1891
D'Odorico, S., Cristiani, S., Dekker, H., et al. 2000, in Society of Photo-Optical Instrumentation Engineers (SPIE) Conference Series, Vol. 4005, Discoveries and Research Prospects from 8- to 10-Meter-Class Telescopes, ed. J. Bergeron, 121–130, doi: 10.1117/12.390133
Eisenstein, D. J., Zehavi, I., Hogg, D. W., et al. 2005, ApJ, 633, 560, doi: 10.1086/466512
El-Badry, K. 2019, MNRAS, 482, 5018, doi: 10.1093/mnras/sty3109
El-Badry, K., & Rix, H.-W. 2018, MNRAS, 480, 4884, doi: 10.1093/mnras/sty2186
El-Badry, K., Rix, H.-W., & Heintz, T. M. 2021, MNRAS, 506, 2269, doi: 10.1093/mnras/stab323
Famaey, B., & Binney, J. 2005, MNRAS, 363, 603, doi: 10.1111/j.1365-2966.2005.09474.x
Famaey, B., & McGaugh, S. S. 2012, Living Reviews in Relativity, 15, 10, doi: 10.12942/lrr-2012-10
Gaia Collaboration, Prusti, T., de Bruijne, J. H. J., et al. 2016, A&A, 595, A1, doi: 10.1051/0004-6361/201629272
Gaia Collaboration, Brown, A. G. A., Vallenari, A., et al. 2021, A&A, 649, A1, doi: 10.1051/0004-6361/202039657
Gaia Collaboration, Vallenari, A., Brown, A. G. A., et al. 2023, A&A, 674, A1, doi: 10.1051/0004-6361/202243940
Gelman, A., & Rubin, D. B. 1992, Statistical science, 7, 457
Gentile, G., Famaey, B., & de Blok, W. J. G. 2011, A&A, 527, A76, doi: 10.1051/0004-6361/201015283
Hartman, Z. D., & Lépine, S. 2020, ApJS, 247, 66, doi: 10.3847/1538-4365/ab79a6
Hernandez, X. 2023, MNRAS, 525, 1401, doi: 10.1093/mnras/stad2306
Hernandez, X., Chae, K.-H., & Aguayo-Ortiz, A. 2024a, MNRAS, 533, 729, doi: 10.1093/mnras/stae1823
Hernandez, X., Cookson, S., & Cortés, R. A. M. 2022, MNRAS, 509, 2304, doi: 10.1093/mnras/stab3038
Hernandez, X., Jiménez, M. A., & Allen, C. 2012, European Physical Journal C, 72, 1884, doi: 10.1140/epjc/s10052-012-1884-6
Hernandez, X., Verteletskyi, V., Nasser, L., & Aguayo-Ortiz, A. 2024b, MNRAS, 528, 4720, doi: 10.1093/mnras/stad3446
Hoffman, M. D., Gelman, A., et al. 2014, J. Mach. Learn. Res., 15, 1593
Hopkins, A. M. 2018, PASA, 35, e039, doi: 10.1017/pasa.2018.29
Hwang, H.-C., El-Badry, K., Rix, H.-W., et al. 2022a, ApJL, 933, L32, doi: 10.3847/2041-8213/ac7c70
Hwang, H.-C., Ting, Y.-S., & Zakamska, N. L. 2022b, MNRAS, 512, 3383, doi: 10.1093/mnras/stac675
Katz, D., Sartoretti, P., Guerrier, A., et al. 2023, A&A, 674, A5, doi: 10.1051/0004-6361/202244220
Kumar, R., Carroll, C., Hartikainen, A., & Martin, O. 2019, The Journal of Open Source Software, 4, 1143, doi: 10.21105/joss.01143
Langford, Z., Blake, C., Halverson, S., et al. 2025, arXiv e-prints, arXiv:2510.16139, doi: 10.48550/arXiv.2510.16139
Lelli, F., McGaugh, S. S., Schombert, J. M., & Pawlowski, M. S. 2016, ApJL, 827, L19, doi: 10.3847/2041-8205/827/1/L19
Liu, F., Ting, Y.-S., Yong, D., et al. 2024, Nature, 627, 501, doi: 10.1038/s41586-024-07091-y
McGaugh, S. S. 2011, PhRvL, 106, 121303, doi: 10.1103/PhysRevLett.106.121303
—. 2016, ApJL, 832, L8, doi: 10.3847/2041-8205/832/1/L8
Meléndez, J., Asplund, M., Gustafsson, B., & Yong, D. 2009, ApJL, 704, L66, doi: 10.1088/0004-637X/704/1/L66
Metchev, S. A., & Hillenbrand, L. A. 2009, ApJS, 181, 62, doi: 10.1088/0067-0049/181/1/62
Milgrom, M. 1983a, ApJ, 270, 371, doi: 10.1086/161131
—. 1983b, ApJ, 270, 384, doi: 10.1086/161132
Nelson, T., Ting, Y.-S., Hawkins, K., et al. 2021, ApJ, 921, 118, doi: 10.3847/1538-4357/ac14be
Oh, S., Price-Whelan, A. M., Hogg, D. W., Morton, T. D., & Spergel, D. N. 2017, AJ, 153, 257, doi: 10.3847/1538-3881/aa6ffd
Oort, J. H., & Rougoor, G. W. 1960, MNRAS, 121, 171, doi: 10.1093/mnras/121.2.171
Pittordis, C., & Sutherland, W. 2018, MNRAS, 480, 1778, doi: 10.1093/mnras/sty1578
—. 2023, The Open Journal of Astrophysics, 6, 4, doi: 10.21105/astro.2205.02846
Planck Collaboration, Aghanim, N., Akrami, Y., et al. 2020a, A&A, 641, A1, doi: 10.1051/0004-6361/201833880
—. 2020b, A&A, 641, A6, doi: 10.1051/0004-6361/201833910

Pontzen, A., & Governato, F. 2012, MNRAS, 421, 3464, doi: 10.1111/j.1365-2966.2012.20571.x

Rao, C. R., et al. 1945, Bull. Calcutta Math. Soc, 37, 81

Rubin, V. C., & Ford, Jr., W. K. 1970, ApJ, 159, 379, doi: 10.1086/150317

Rubin, V. C., Ford, Jr., W. K., & Thonnard, N. 1980, ApJ, 238, 471, doi: 10.1086/158003

Saglia, R., Pasquini, L., Patat, F., et al. 2025, A&A, 699, A151, doi: 10.1051/0004-6361/202555115

Salvatier, J., Wiecki, T., & Fonnesbeck, C. 2015, arXiv e-prints, arXiv:1507.08050, doi: 10.48550/arXiv.1507.08050

Sanders, R. H. 2003, MNRAS, 342, 901, doi: 10.1046/j.1365-8711.2003.06596.x

—. 2015, Canadian Journal of Physics, 93, 126, doi: 10.1139/cjp-2014-0206

Sanders, R. H., & McGaugh, S. S. 2002, ARA&A, 40, 263, doi: 10.1146/annurev.astro.40.060401.093923

Sofue, Y., & Rubin, V. 2001, ARA&A, 39, 137, doi: 10.1146/annurev.astro.39.1.137

Springel, V., White, S. D. M., Jenkins, A., et al. 2005, Nature, 435, 629, doi: 10.1038/nature03597

Sun, Q., Ting, Y.-S., Anthony-Twarog, B. J., et al. 2025a, ApJ, 991, 185, doi: 10.3847/1538-4357/adfccd

Sun, Q., Ting, Y.-S., Liu, F., et al. 2025b, ApJ, 978, 107, doi: 10.3847/1538-4357/ad8dc3

Tian, H.-J., El-Badry, K., Rix, H.-W., & Gould, A. 2020, ApJS, 246, 4, doi: 10.3847/1538-4365/ab54c4

Valle, G., Dell'Omodarme, M., Prada Moroni, P. G., & Degl'Innocenti, S. 2013, A&A, 549, A50, doi: 10.1051/0004-6361/201220069

—. 2014, A&A, 561, A125, doi: 10.1051/0004-6361/201322210

Vogt, S. S., Allen, S. L., Bigelow, B. C., et al. 1994, in Society of Photo-Optical Instrumentation Engineers (SPIE) Conference Series, Vol. 2198, Instrumentation in Astronomy VIII, ed. D. L. Crawford & E. R. Craine, 362, doi: 10.1117/12.176725

Weinberg, D. H., Bullock, J. S., Governato, F., Kuzio de Naray, R., & Peter, A. H. G. 2015, Proceedings of the National Academy of Science, 112, 12249, doi: 10.1073/pnas.1308716112

Wetzel, A. R., Hopkins, P. F., Kim, J.-h., et al. 2016, ApJL, 827, L23, doi: 10.3847/2041-8205/827/2/L23

Yong, D., Liu, F., Ting, Y.-S., et al. 2023, MNRAS, 526, 2181, doi: 10.1093/mnras/stad2679

Yu, J., Ting, Y.-S., Casagrande, L., et al. 2025, MNRAS, 538, 2408, doi: 10.1093/mnras/staf436

Zhao, H. S., & Famaey, B. 2006, ApJL, 638, L9, doi: 10.1086/500805

Zwicky, F. 1937, ApJ, 86, 217, doi: 10.1086/143864